Effects of Thermal Gradient and Cyclic Oxidation on the Delamination and Lifetime of High temperature Protective Coatings

Shuhong Dong

Thesis submitted to the University of Ottawa
in partial Fulfillment of the requirements for the Master of Applied Science-
Advanced Materials and Manufacturing

Department of Mechanical Engineering
Faculty of Engineering
University of Ottawa

ABSTRACT

Thermal barrier coatings have been widely used to provide thermal protection to components in the hot section of gas turbines. This research focuses on two influencing factors on coating behavior: thermal gradient and cyclic oxidation.

The delamination mechanics under thermal gradient is analyzed, taking thermally grown oxide into consideration. Coatings experience thermal gradients at different stages during actual service flight. One is due to engine power shut down when landing and the other due to internal cooling of the substrate. Thermally grown oxide (TGO) also acts as a critical factor in delamination mechanics. The induced stress gradient and corresponding energy release rate for interface delamination and shallower delamination are presented. Mechanism maps that explain the criteria for preventing delamination from developing and propagating are established. Three cooling trajectories are envisaged to analyze the variation in the possibility of delamination.

Multilayer coatings used in components of the hot section of aero turbine engines also experience cyclic temperature variation during flight cycles. As experiment conditions vary and coating performance is improved, the time required to run through the test of coating failure can be both time-consuming and prohibitive. Therefore, protocols providing prediction of quantified coating behavior are in demand to shorten life-time tests. Curves of mass change are obtained from quantifying scale growth and loss by different models such as Cyclic Oxidation Spall Program (COSP). A modification is made by combining COSP and a mechanic based model to obtain critical parameters for lifetime prediction from short time experiment. The time for coatings to reach peak temperature during cycling is discovered to influence prominently on modeling results. Predictions for several coating compositions and cycling conditions are consistent with the data from the existing experiments of the coating system.

Keywords: thermal barrier coatings, thermal gradient, thermally grown oxide, spherical symmetry, delamination location, mechanism map, cyclic oxidation, weight change, life-time

ACKNOWLEDGEMENTS

I would like to express my appreciation to my supervisor, Ming Liang, who read and gave elaborate suggestions of the thesis and co-supervisor Kuiying Chen who provided insight and expertise towards the research.

Thank you for your guidance and support, your assistance is priceless.

I would also like to show my gratitude to Bochun Zhang and Wentian Wang, who generously shared their experiences and helped a lot with preparing the seminar.

I am also immensely grateful to the thesis examiners for their time and precious advice.

And finally, thanks to my parents and friends for their company and love all this time.

LIST OF FIGURES AND TABLES

LIST OF ABBREVIATION

APS	Air Plasma Spray
BC	Bond Coat
CTE	Coefficient of Thermal Expansion
COSP	Cyclic Oxidation Spall Program
DICOSM	Deterministic Interfacial Cyclic Oxidation Spall Model
EB-PVD	Electron Beam Physical Vapor Deposition
MC	Monte Carlo
TBC	Thermal Barrier Coating
TGO	Thermally Grown Oxide
TGA	Thermogravimetric Apparatus
UL	Uniform Layer

TABLE OF CONTENTS

CHAPTER 1. INTRODUCTION

1.1Introduction to TBC system:

The engine components of aircraft are required to perform reliably under the tough conditions of high temperature and heating cycles. Various approaches have been put into practice to improve the high temperature durability of gas turbine and aero-engine parts, especially turbine blades which must withstand mechanical loads and high temperature exposure. Thermal barrier coatings (TBCs) are a highly advanced material system. They provide insulation to components during large, long-term heat loads and substantially raise the permitted gas temperature above that of uncoated systems. Due to the ever-increasing demands for jet-engine combustion temperature and operating pressure, improved characteristic and a longer life-time of TBC are required [16].

1.1.1 TBC system composition

The TBC system consists of four primary constituents: a yttria stabilized zirconia ceramic top coat that insulates heat from the system, an inter-metallic bond coat (BC) that provides protection against oxidation and hot gas corrosion, a layer of thermally grown oxide (TGO), predominantly alumina, between the ceramic top coat and metallic bond coat, and a Nickel based super-alloy substrate [2]. The bond coat contains enough aluminum to react with oxygen in preference to other oxide and thus forms the TGO, which has a lower oxygen diffusivity and superior adherence, providing protection from further oxidation and separation.

1.1.2 TBC preparation

In industry, thermal barrier coatings are prepared by a variety of approaches such as air plasma spraying (APS), electron beam physical vapor deposition (EB-PVD), high velocity oxygen

fuel (HVOF), suspension plasma spray (SPS) [4] [5], and direct vapor deposition. The preferred methods are currently APS and EB-PVD. For APS, it has the advantage of economically producing reproducible and durable coatings in a large area. Briefly, solid particles are injected into a plasma jet, then heated and melted. The molten parts are then accelerated by an electrostatic field and deposited on the substrate. The APS coating normally has a lamellar morphology with micro-cracks and high porosity, which results in lower thermal conductivity [6]. The connection of the micro-cracks and porosity allows the TBCs to be strain tolerant to avoid scale delamination [3].

The electron beam physical vapor deposition process is another widely applied technology for coating preparation. In this process, an electron beam with a high kinetic energy is used to heat and vaporize coating material. Coatings deposited by EB-PVD usually exhibit a structure of column with porosity inside each column, permitting higher strain tolerance and much longer thermal cycle lifetime. Different from APS, a smooth interface between the bond coat and the ceramic is required, rather than a rough interface.

1.1.3 Failure mechanism

Prolonged high temperature and oxidation exposure will lead to thermal barrier coating failure due to the influence of many complicated factors. Extensive studies have been performed to better understand the failure mechanisms and many factors are found to have an impact on the failure of the system, such as coating thickness [7], coating composition, exposure environment and bond coat fabrication procedure. The main factors widely considered include stress caused by the coefficient of thermal expansion (CTE) mismatch between ceramic topcoat and metallic layer, ceramic sintering and creep, and the growth of TGO, as described in the following.

Thermal expansion mismatch

Thermal expansion is the increase in the volume of a material as its temperature is increased. It varies from material to material due to the difference in bonding forces among atoms and

molecules. The expansion mismatch between two materials can result in significant residual stresses.

Due to the CTE variation between the ceramic coating and metallic substrate, the amount of deformation from the top coat and substrate differentiates under thermal cycling. Therefore, a considerable thermal stress is induced. A layer of bond coat is added to lighten the mismatch effect and improve the system's resistance to oxidation and corrosion.

Sintering and creep

In service, thermal barrier coatings are exposed to oxidizing combustion gas and a temperature as high as 1200℃. Under these tough conditions, temperature dependent phenomena can occur. For example, sintering of the ceramic top coat is often observed. During sintering, atoms diffuse across the boundaries of the particles, causing the microstructure of the top coat to change. The phenomenon causes a further change of thermal conductivity and Young's modulus, which results in the decrease of coating's resistance to defect. The variations of properties will finally bring about the early formation and aggravation of the delamination.

TGO growth

Upon high temperature exposure to oxygen, a thin layer of thermally grown oxide forms between the ceramic coating and aluminum-rich bond coat [8].It provides protection to the substrate from further oxidation. During high temperature operation, the TGO thickens with time and follows a parabolic growth law. The increase in TGO thickness can be the cause of different failure mechanisms: (i) The large stress in TGO leads to the extension of the interface and forms an undulated morphology which induces high stresses that cause micro-cracks to emerge; and (ii) The interface between TGO and BC tends to debond due to stored elastic strain energy in the TGO/BC bi-layer.

The critical role that TGO plays in coating failure has led to insightful studies of the complicated combination of various factors that control TGO stress field and morphology [9].

1.1.4 Cyclic Oxidation

Intermetallic alloys make up an important part of the gas turbine in the engine of aircraft. They play a vital role in achieving higher durability of the engine, especially under cyclic temperature variation due to aircraft taking off and landing. The maximum temperature of the working components can reach around 1200℃. Therefore, there can be a more complicated pattern of oxidation which causes the surface layer of the material to fall off and fail. Cyclic oxidation is an important type of test to assess the material's environment durability under repeated heating and cooling. A large amount of information for oxidation under isothermal conditions is provided by isothermal thermogravimetric analysis (TGA). However, it does not inspire ideas on the mechanisms controlling cyclic oxidation. To better understand the laws of cyclic oxidation, mechanistic models have been developed to quantitatively describe the scale growth and loss, and to obtain the weight change curve in the same manner as actual experimental results [10][11][12][14].

The main purpose of the life prediction is to estimate the extent to which the coating degrades during repeated heating conditions [15]. The most challenging part is to measure the metal consumption during each cycle, which would be of great difficulty and lead to poor accuracy if obtained from experiments. The most applied models in this investigation are cyclic oxidation spall program (COSP), including uniform layer version (UL) and Monte Carlo version (MC) [13], and deterministic interfacial cyclic oxidation spall model (DICOSM)[10]. The models follow the same rule of oxide growth during heating cycles. The difference between the models lies in how they describe the spallation mode during cooling.

The iterative process of the COSP UL model is described in Fig. 1-1(A). The oxide grows a complete layer, following a pre-described growth law. The growth rate is a function of the oxide thickness at the instant. The amount of spallation in each cycle only depends on the amount of oxide existing after each heating process.

In the Monte Carlo modeling version, as shown in Fig. 1-1(B), the surface is divided into separated areas and each area experiences oxide growth and spallation individually. The oxide

is allowed to spall completely to the bare metallic substrate, which is closer to actual conditions rather than spalling just a layer of the surface. Fig. 1-1 (C) shows and example of DICOSM modelling, which is described in section 2.4.

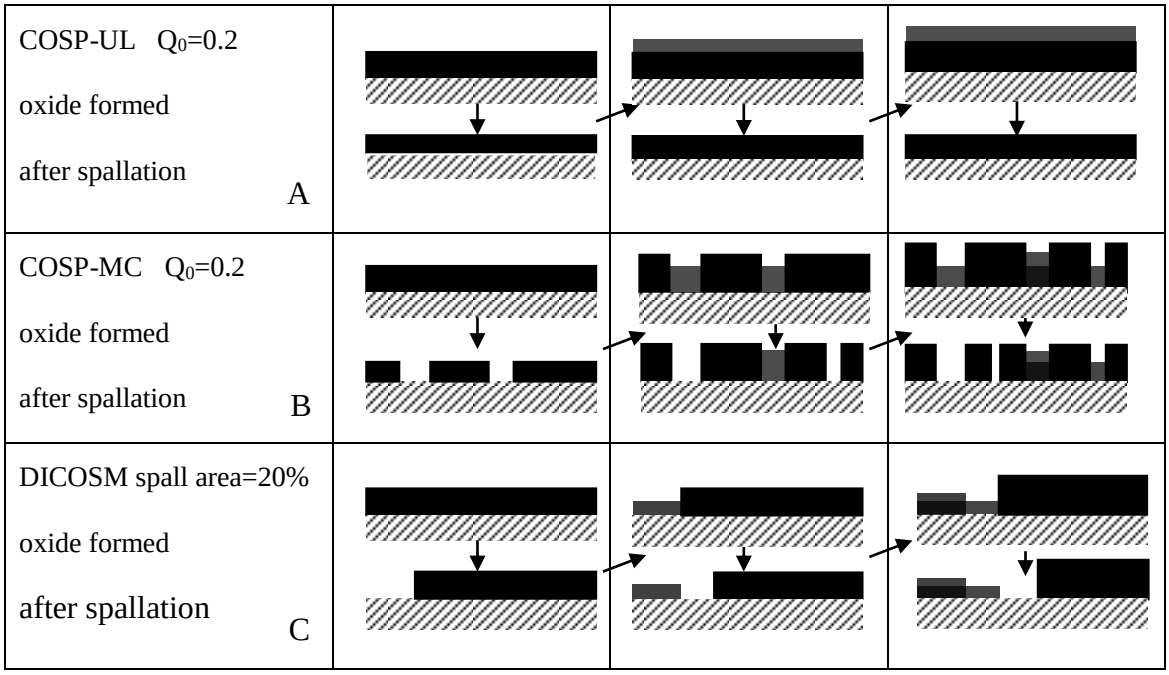

Fig. 1-1 Spallation modes of different modeling approaches [10].

1.2 Objectives and contribution of the thesis

This thesis aims to improve the existing model in analyzing the delamination mechanics of thermal barrier coating under thermal gradient and to to propose a model to predict the cyclic oxidation behaviour with higher efficiency.

For thermal gradient modeling, our goal is to mitigate delamination in the coating. Dependence between substrate temperature change and surface temperature change is used to give a better explanation of the criteria to prevent delamination initiation and propagation. Thermally grown oxide and the interface's irregularity are also taken into consideration to yield more accurate predictions. The delamination maps indicate the result of different temperature trajectories of turbines and provide ideas of safe service that avoide delamination from forming and propagating. The modified model takes the critical TGO effect into consideration which makes it more complete theoratically and more promising to give an

accurate prediction of delamination incidence.

A modification based on an existing mechanic based model of cyclic oxidation is proposed to optimize coating life time prediction. The improvement is made by introducing a critical variable, time to reach maximum weight change, into the iterative modeling approach. The coating's weight change over long time can then be predicted using significantly less experimental data which is beneficial both in time and cost. Due to the sensitivity of the variable to the data implicated, and the neglected dependence of coating's properties such as Young's modulus, there can be certain limitations to the conditions that can be applied for satisfactory results.

CHAPTER 2. THE LITERATURE REVIEW

2.1 **TBC and thermal gradient: sintering and creep**

Plasma-sprayed ceramic TBC have been developed to ensure higher durability and efficiency for gas turbine and diesel engine. However, the failure and coating lifetime under thermal cycling remains a vital problem. Among all causes of failure, ceramic top coat sintering and creep can result in coating shrinkage and through-thickness cracks. Many studies have been carried out to investigate the mechanism controlling coating behaviour under these conditions. A unique approach has been presented by Zhu and Miller [20] to quantitatively determine sintering, creep behavior and coating pressure under heat flux. Also, for temperature and stress distributions under laser conditions, Young's modulus, stress response and accumulated creep strain have been simulated.

Under laser heating conditions, a sharp temperature gradient and thus a stress gradient are introduced into the ceramic top coat. Backside air cooling is employed to set up the temperature gradient. The temperature and stress gradients hinge on factors including laser heat flux, surface temperature, material properties and configurations of the coating systems [20]. The creep strain rate under laser induced temperature and in-plain thermal stress is a function of stress rate, coating temperature and time.For this situation, the strain rate with constant modulus is can be expressed using and iterative equation that steps through time instances as:

$$\dot{\varepsilon}_p^i = A \cdot \exp(-\frac{Q}{RT}) \cdot \{\sigma_0 - \varepsilon_p^{i-1} \frac{E_c}{1-\nu_c}\}^n \cdot t_i^{-s} \tag{2-1}$$

where $\dot{\varepsilon}_p^i$ and ε_p^{i-1} are the creep strain at time, t_i ,and the total accumulated strain at the previous time step t_{i-1} respectively, σ_0 is the initial thermal stress in the coating, E_c and ν_c are elastic modulus and Poisson's ratio of the top coating, *Q* is the activation energy, *n*

and *s* are the stress and time exponent. The opening rate and penetration depth change of a crack during laser heating is a prerequisite for determining creep behavior. In laser experiments, the creep strains are derived from crack opening displacements at different depths after cooling and the actual creep strain rates are determined from derivatives of curves plotted by creep strain over experiment time [39].

From equation (2-1), the strain rate variation in regard to time and temperature can be obtained. Plotting $\partial \ln \dot{\varepsilon}_n^t(T,t)/\partial t$ vs. 1/*t*, the slope of $\partial \ln \dot{\varepsilon}_n^t(T,t)/\partial t$ *v*s.$1/t$ gives the exponent of time, *s*. The stress exponent *n* can be derived from surface stress relaxation rate and differential strain rate change. The parameter, *Q*, is the activation energy, which can be obtained from the slopes of strain rate change curve and stress relaxation curve.

In this study, specimens experienced continuous heating for 1hour, 11hours, 22hours or 120hours. Through-thickness cracks mentioned above appeared in all specimens after tests. Coating porosity decreased particularly near the surface, due to high temperature and compressive stress. Porosity gradients through the coating are hard to decide and porosity reduction is believed to be related to creep strain gradients. The micro-crack density near the surface appeared to be much lower than that near TBC-BC interface.

The creep strain gradient resulting from laser-imposed temperature and stress gradient as a function of laser testing time is shown in Fig.2-1-1. The creep strain increases rapidly at first and then experiences a much lower increase rate in longer time[20]. With the distance from the surface increasing, creep strains decrease.

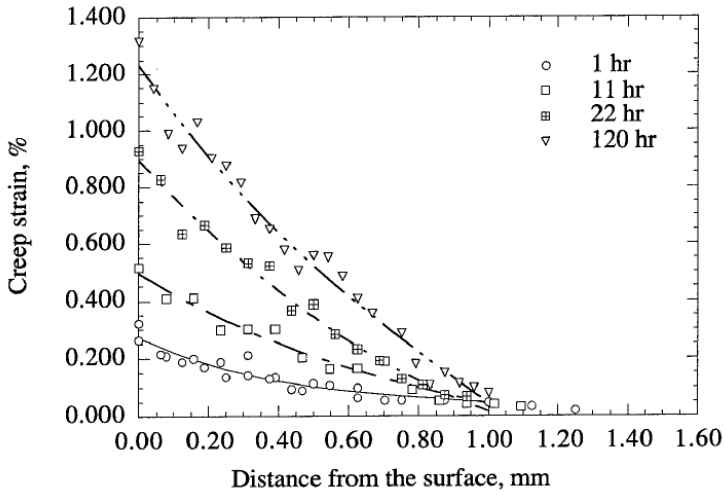

Fig.2-1-1 Creep strain through the coating after sintering and creep test [20].

Experimental data are fitted in following forms and shown in Fig.2-1-2.

$$\dot{\varepsilon}_p(T,t) = A(T)\cdot t^{-s_m}$$

$$\varepsilon_p(T,t) = \frac{A(T)}{1-s_m}\cdot t^{1-s_m} \quad \Delta T(\eta) = (1+c_1\eta)\Delta T_{sur/sub} + \Delta T_{substrate} \tag{2-2}$$

where $A(T)$ is a constant depending on temperature, s_m and $1-s_m$ are time exponents measured from experiments for the strain equation. The exponent, s_m, approaches a constant value of about 0.67 with increasing coating depth and decreasing temperature, this value is taken as *s*. The trend of creep strain and time exponent is shown in Fig.2-1-2.

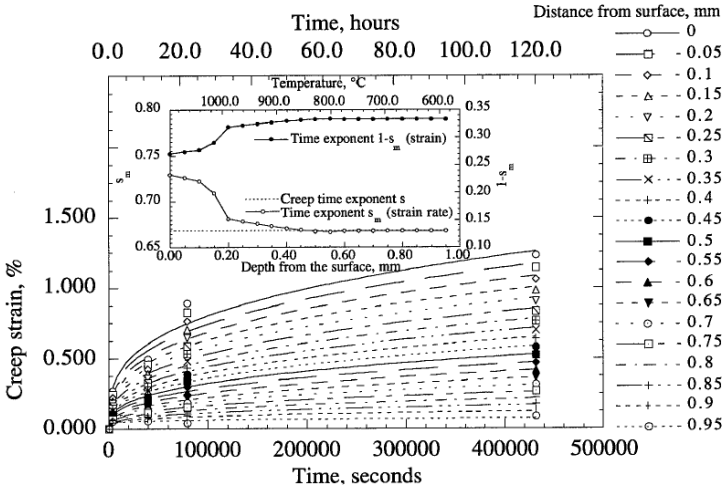

Fig.2-1-2 Creep strain evolution over time across coating depth [39].

It reveals that the creep strain follows an upward trend with time but decreases with temperature. s_m approaches s in the inner layer of the coating, where the temperature is relatively low.

During laser sintering, coating modulus is expected to increase, and the modulus near the surface shows the shortest relaxation time due to the highest temperature. Thermal conductivity also increases as a function of test time and temperature. However, the slight change in conductivity implies surface temperature is approximately fixed.

Elastic stress and creep strain distribution in the coating are simulated. As shown in Fig.2-1-3, the results show significant creep strains and stress relaxation near the surface.

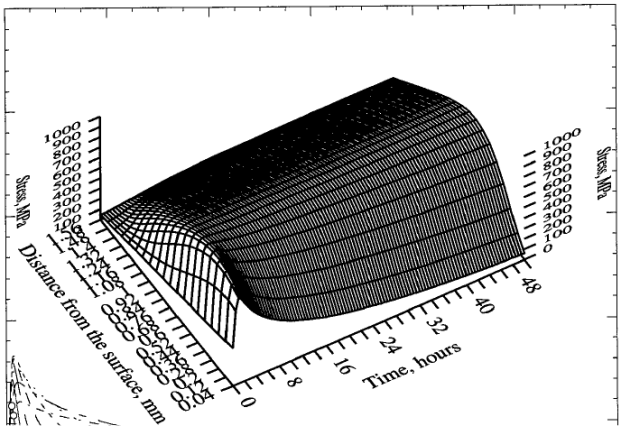

Fig.2-1-3 3D plotting of relationship between creep strain, stress and creep rate with time [39].

The creep strain gradients generated by laser creep tests also show a much higher value at the surface than the inner layer. Modeling results also indicate a decreasing creep strain rate. All the modeled behavior agrees with experimental researches.The modeling approach provides a promising innovation of coating design, life time prediction and stress modeling.

For further investigation into the coating elastic modulus increase during coating sintering, studies based on a laser flux test approach are performed by Zhu and Miller [20] to investigate the evolution of elastic modulus and thermal conductivity.

The modulus variation under the temperature and stress conditions is expressed as:

$$\frac{E_c^{\infty} - E_c}{E_c^{\infty} - E_c^{0}} = \exp[-\frac{t}{\tau}] \tag{2-3}$$

It can be considered as the process of relaxation. E_c^{∞} and E_c^{0} are coating moduli at a

sufficiently long time and at initial time respectively, and τ is a relaxation time, which can be a function of temperature and stress.

For a penny-shaped crack in the ceramic coating parallel to the surface, fracture behavior is investigated by Qian and Nakamura including thermal gradient and residual stress [25]. Also, an embedded through thickness crack is studied.

The following mechanical features are revealed by Qian and Nakamura:

1. The area near the crack tip is discovered to be shear-dominant.
2. Residual stresses are shown to be small for parallel cracks but cracks perpendicular to the surface have a more significant influence on reducing the energy release rate.
3. For a small crack, the energy release rate reaches a maximum value in the middle field of the coating, but for a long crack the value is reached near the ceramic-bond coat interface.

In their study, the surface coating is chosen as ZrO_2+6%wt%Y_2O_3, and the bond coat as NiCrAlY [25]. The 3D temperature contours are shown in Fig.2-1-4 and a steep temperature jump across the crack can be observed. For coating field sufficient away from the crack tip, the temperature distribution can be considered linear with distance from the surface.

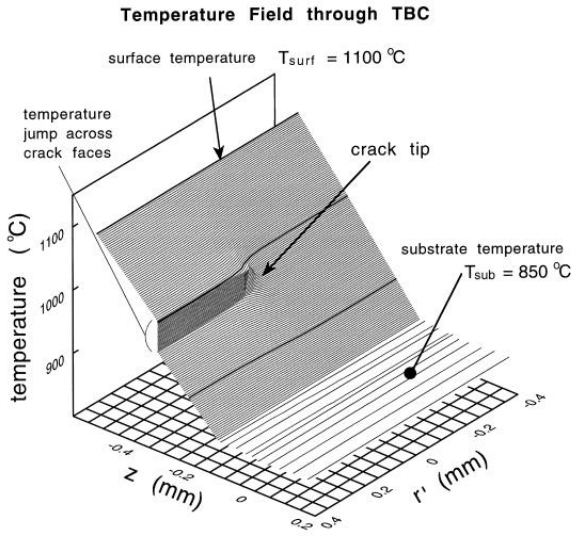

Fig.2-1-4 Temperature distribution through coating thickness with parallel crack [25].

Firstly, a linear elastic model is considered, assuming all materials to be linearly elastic. For interface crack at the interface of the top coat and bond coat and shallower crack located within the ceramic coating, the energy release rate is shown as a function of the surface temperature in Fig.2-1-5, where *a*, the crack radius is set as 2mm. It shows that *G* increases with temperature and the energy release rate of interface crack is around twice that of the crack located in the ceramic coating.

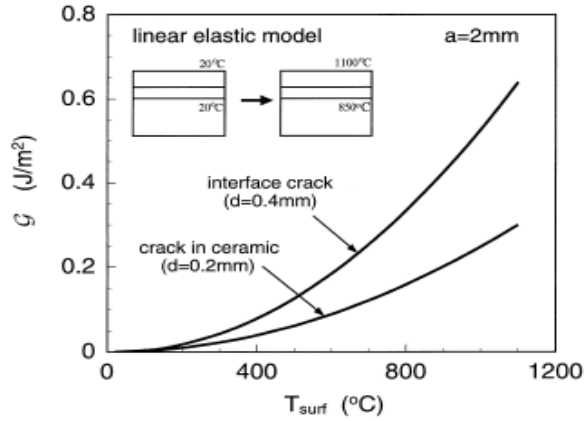

Fig.2-1-5 Relationship of energy release rate with surface temperature (a = 2mm) [25].

In addition, an elastic-plastic model is considered in their work. In this case, both temperature-independent model and temperature-dependent model are investigated. The results of the energy release rate in the temperature-independent model are plotted in Fig.2-1-6. The energy release rate of interface crack is significantly lower compared with the *G* in the linear model which can be attributed to the relaxation of internal stresses due to plastic flow in the bond coat.

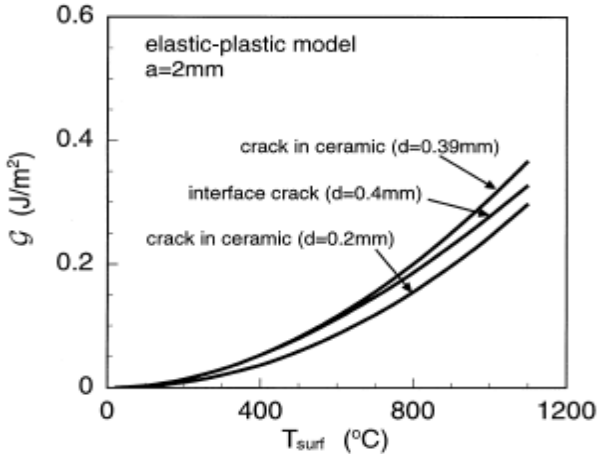

Fig.2-1-6 Energy release rate of temperature-independent elastic-plastic models [25].

Also, *G* with residual stresses is plotted against surface temperature. The energy release rates for cases with the different crack locations and orientation are also obtained, as shown in Fig.2-1-7.

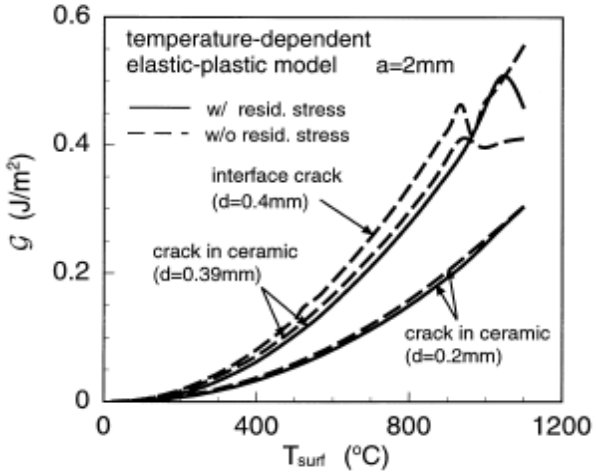

Fig.2-1-7 Energy release rate of temperature-dependent elastic-plastic model with different crack locations (with and without residual stress) [25].

It is revealed that for crack that is sufficiently away from top coat-bond coat interface, the energy release rate is nearly identical for temperature-dependent, temperature independent, linear elastic model and the model with residual stress. However, the bond coat plasticity can be vitally important to the fracture behavior for coating with interfacial cracks.

2.2 **Thermal fracture of TBC under thermal shock test**

The spallation resistance of APS sprayed TBCs with pre-existing cracks has been studied. The microstructure of the deposited APS coating is found to have yttriastabilized zirconia splats, separated by cracks. Also, about 15% of the coating volume is occupied by pores. Inter-splat sintering is found to cause depth-dependent modulus increase and thus an increase in energy release rate [2,3]. In addition, interfacial toughness degrades with time.

In Fleck and Cocks' study [40], the temperature distribution is considered to be linear through the coating as:

$$T(y) = T_I + (T_S - T_I)\frac{y}{h} \tag{2-4}$$

where T_s and T_I are the temperatures of the surface and interface respectively. The temperature change history in the heating/cooling cycle is shown in Fig.2-2-1. This temperature history simulates the process of engine shut-down and restarts.

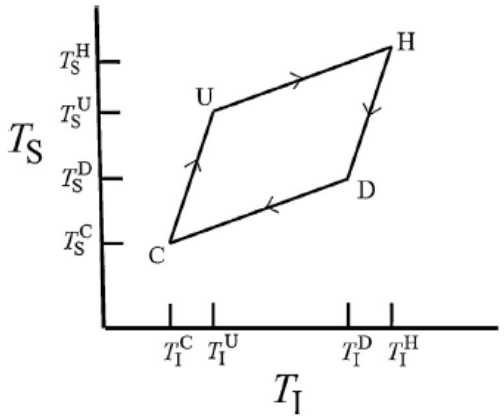

Fig.2-2-1 The temperature history of coating: H is the initial hold temperature, C is the cool state temperature, D and U are intermediate temperatures during cooling and reheating [40].

The in-plane stress during the cycle is given as:

$$\sigma(y)=\frac{E(y)}{(1-v)}[\alpha_{TBC}(T^H(y)-T(y))+\alpha_{SUB}(T_I-T_I^H)] \tag{2-5}$$

where α_{TBC} and α_{SUB} are the thermal expansion coefficients of the ceramic coating and substrate, respectively.The evolution of in-plane modulus at T_H in an unsupported coating is investigated. *E* is found to increase with sintering time.

The mode I and mode II interfacial stress intensity factors are given as:

$$K_I=0.434\frac{P}{\sqrt{\hat{A}h}}+0.558\frac{M}{\sqrt{\hat{I}h^3}},K_{II}=0.558\frac{P}{\sqrt{\hat{A}h}}-0.434\frac{M}{\sqrt{\hat{I}h^3}} \tag{2-6}$$

where the dimensionless quantities $\hat{A}$ and $\hat{I}$ describes the equivalent section. For example, for a rectangular section of homogeneous coating, $\hat{A}=1$ and $\hat{I}=1/12$. P and M are respectively the end load and bending moment that act on the neutral axis of the equivalent section.

In terms of toughness, the criterion of delamination can be expressed as:

$$\hat{G} \equiv \frac{G(\psi)}{\Gamma_{IC}}[\cos^2\psi + \frac{\Gamma_{IC}}{\Gamma_{IIC}}\sin^2\psi] = 1 \tag{2-7}$$

where Γ_{IC} and Γ_{IIC} are the mode I and mode II fracture toughness respectively, ψ is the phase angle of loading. Delamination is expected when $\hat{G}$ reaches unity in the cycle. The value of Γ_{IC}/Γ_{IIC} is given in the previous study as 0.11 and 0.23, Γ_{IC}/Γ_{IIC} is taken as 0.17 in Fleck's study [40].

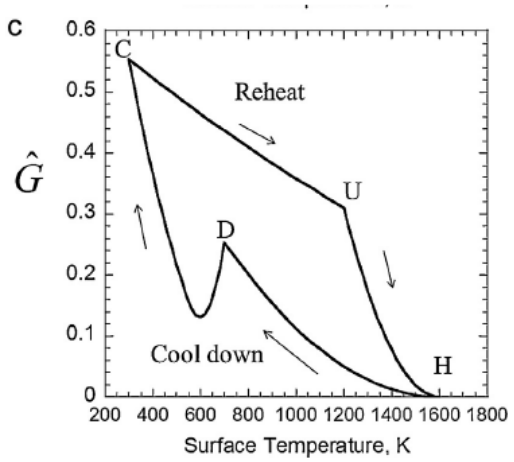

Fig.2-2- 2 Crack tip driving force during cooling/heat cycle [40].

The change of $\hat{G}$ during cooling and heating cycle is given in Fig.2-2- 2 and the maximum is obtained at T_c, the lowest temperature of the cycle. Therefore, in this case, to assess whether the delamination occurs, we only need to evaluate the energy release rate when the coating is in the cold state.

Based on the results from previous laser thermal shock experiments and principles of crack arrest, the crack resistance of a thermal barrier coating is investigated by Rangaraj and Kokini [41]. A functionally graded TBC, which has a changing composition through the coating, is considered. Fracture resistance curves are presented for cracks emerging at the coating surface and propagating perpendicularly to the layers.

High heat flux load leads to relatively long crack at the TBC surface and near the interface of the ceramic coating and bond coat. Functionally graded TBCs are developed to enhance fracture resistance. This composition changes through the thickness. The graded TBC is

observed to have lower driving force and higher fracture toughness for interface cracks. Mostly, fracture toughness, to a large extent, depends on the crack extension. In other words, crack resistance changes with crack length. It has been reported that fracture resistance is enhanced along the direction of coating composition gradation [41].

TBCs with one, three, six and nine layers of top coat were considered in this study. Each specimen experienced one single cycle of heating and cooling. For surface cracks, the final crack lengths are plotted as a function of the maximum surface temperature shown in Fig.2-2-3. The specimens with similar final crack lengths experience different maximum surface temperature.

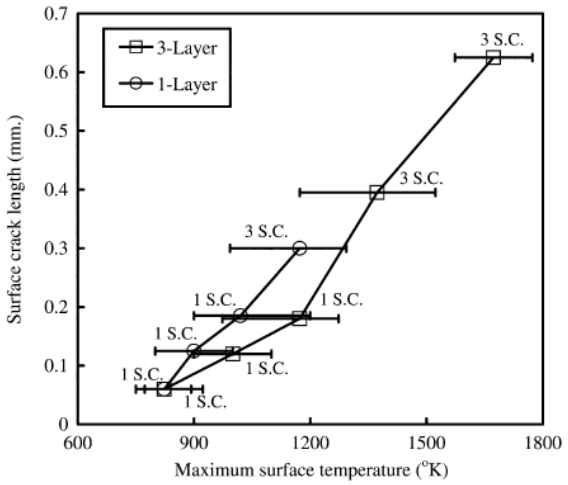

Fig.2-2- 3 Surface crack length as a function of maximum surface temperature for coating with one and three layers [41].

Also, for a crack initiating at the surface and with perpendicular propagation, the strain energy release rate is shown in Fig.2-2-4 as a function of crack length. For resistance to the growth of surface cracks, the curve suggests a temperature sensitive property, which means that a small temperature increase will result in a significant rise in surface crack energy release rate.

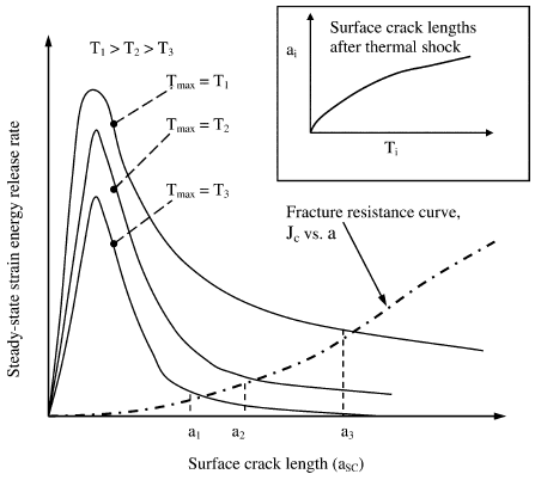

Fig.2-2-4 Energy release rate based illustration of crack growth and arrest with various T_{max} [41].

TBCs with more layers show higher fracture resistance. It is considered for two reasons: increased fracture toughness due to the addition of bond coat and a longer crack propagated to reach more layers of the graded TBC.

For a coating with constant surface temperature, the effect of coating thickness on thermal fracture behavior under high heat flux is identified by Choules and Kokini [43]. High heat flux heating is found to lead to denser coating microstructure and stress relaxation. Thus it causes surface and interface cracks to develop during a cooling process. Coating thickness is found to affect surface cracks in number, length and interval. When coating thickness increases, surface cracks are found to decrease in number and increase in their spacing. In addition, the crack extension into coating layer becomes shorter. Higher maximum surface temperatures are found to result in larger surface cracks length. It agrees with the conclusion mentioned above. Also, it has been observed that when coating thickness is increased, more interface cracks start to develop and the trend is reversed after reaching the maximum.[43]

Research based on these results is presented to further investigate the interface thermal fracture in pre-cracked TBCs. Results show that, after a thermal shock process, interfacial cracking decreases as crack density increases. A numerical model was proposed and then applied to study the influence of laser heat flux on interface cracks. [28]

For the analytical model, a few assumptions were made:

(1) all materials are isotropic,

(2) only plane stress condition is considered in the specimen,

(3) temperature is unrelated to the displacements of the body,

(4) perfect bond exists between varied materials and displacements and temperatures are continuous across the interface, and

(5) cracks are perfect heat conductors.

The results show that considering fixed coating thickness, vertical cracks significantly enhance the thermal shock resistance of TBC to interface crack initiation and propagation. The strain energy release rate is fairly small for uncracked coating. However, for a single crack case, it increases rapidly. In the results of thermal stress, it is found that the uncracked coating is most inclined to initiate surface cracks.

With increasing crack density, the lowest temperature for interface cracks to initiate increases. It is shown in Fig.2-2-5 and can be explained by the presence of microcracks. Microcracks reduce *G* during the thermal shock process, therefore, the temperature required for interface crack initiation and propagation becomes higher.

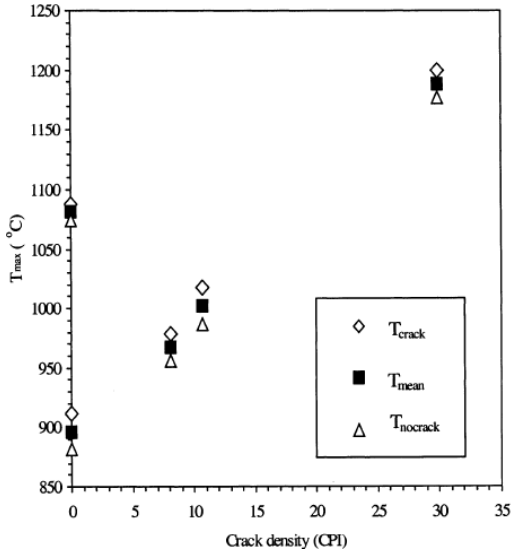

Fig.2-2-5 T_{crack}, T_{mean}, $T_{nocrack}$ over varied crack density (CPI) [42].

Although interface crack development for uncracked coatings occurs at the lowest temperature, it resulted in the largest amount of interface cracking. Coatings with the largest crack densities were determined to have the most thermal load allowance.

From the conclusion of the study, the crack density can be considered as a vital design parameter. Plasma sprayed coatings of high density with vertical cracks are expected to show

enhanced thermal shock resistance.

The thermal shock resistance was analyzed for two types of plates in a brittle solid by Lu and Fleck [44]: (I) a plate containing a distribution of imperfections, and (II) a plate with a single dominant crack in the through-thickness direction. For the two types of plates, a fracture criterion based on local stress and another criterion based on fracture toughness are appropriate respectively. In the cold shock condition, the near surface area of the plate has a tensile stress field and a mode I stress intensity factor rises for a pre-existing crack at the surface. While in the case of hot shock, the location of tensile stress field is at the center of the plate and therefore leads to a mode I stress intensity factor for a pre-existing crack at the center of the plate.

The main feature of Lu and Fleck's study [44] is that, over the full range of Biot number, new non-dimensional parameters for analyzing the thermal shock resistance of a brittle solid are obtained. For the cold shock, edge crack is taken to be the most damaging factor where as for hot shock the factor is considered to be center crack.

Fig.2-2-6 is used to analyze the following phenomenon during thermal shock.

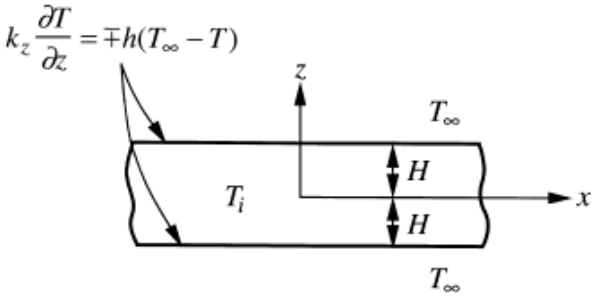

Fig.2-2-6 A finite-thickness plate subjected to a shock of different temperature [44].

In this figure, 2*H* is the thickness of the infinite plate, *h* is the heat transfer coefficient, T_i is the initial temperature of the coating, and the coating surface and bottom are suddenly exposed to temperature T_∞ when the test time starts.Surface heat flow is assumed to follow: $k_z \frac{\partial T}{\partial z} = \mp h(T_\infty - T)$, at $z = \pm H$, *k* is the thermal conductivity of the material in the thickness direction and *h* is the coefficient of heat transfer. The transient thermally-induced stress is:

$$\sigma_{xx}(z,t) = -\bar{E}\bar{\alpha}(T - T_i) + \frac{\bar{E}\bar{\alpha}}{2H}\int_{-H}^{H}(T - T_i)dz \tag{2-8}$$

The temperature distribution takes the form,

$$\frac{T(z,t) - T_i}{T_i - T_\infty} = -1 + \frac{4}{\pi}\sum_{n=0}^{\infty}\frac{(-1)^n}{2n+1} \times \exp(-\frac{(2n+1)^2\pi^2}{4}\frac{\kappa_z t}{H^2}) \times \cos[\frac{(2n+1)\pi}{2}\frac{z}{H}] \tag{2-9}$$

for perfect heat transfer, biot number $B_i = \infty$. In the condition of cold shock, the surface layer experiences a tensile stress transient while the centre of the plate experiences compressive stress. The magnitude of the stresses increases with B_i. It also explains the phenomenon that cracks initiate at the surface and propagates until entering the plate centre with a compressive stress field. However, under hot shock, the center of the plate is under tension and is about to crack.

For cracks induced by cold shock, the crack is expected from the worst flaw which is defined to be the one with the largest mode I stress intensity factor. The intensity factor is given as:

$$\frac{K}{K^0} = \frac{\lambda^{-3/8}}{\sqrt{n}}\frac{2}{\pi\sqrt{a/H}}\int_{1-a/H}^{1}[\frac{F_1(z/H, a/H)\bar{\sigma}(z/H,t)}{(1-a/2H)^{1.5}\sqrt{1-[(H-z)/a]^2}}]d(\frac{z}{H}) \tag{2-11}$$

where $K^0 \equiv \sqrt{\pi H}\bar{E}\bar{\alpha}(T_i - T_\infty)$ is a given as a reference stress intensity factor and F_1 is a dimensionless function. K achieves a peak value at a certain time and then decreases. Furthermore, the magnitude of K depends on the crack length and shows a peak value at a crack length of $a/H \approx 1/3$. $K_{max} = 0.222K^0$ is the largest stress intensity factor for any crack length in the condition of $B_i = \infty$ (Also applicable to an edge crack or a center crack under hot shock).Failure is assumed to occur when K_{max} equals K_{IC} for the solid.

For a hot shock induced crack, the mode I stress intensity factor is given as:

$$\frac{K}{K^0} = \frac{\lambda^{-3/8}}{\sqrt{n}}\sqrt{\frac{2}{\pi}\tan\frac{\pi a}{2H}} \times \int_0^{a/H}[\frac{F_2(z/H, a/H)\bar{\sigma}(z/H,t)}{\sqrt{1-(\cos\frac{\pi a}{2H}\cos\frac{\pi}{2}\frac{z}{H})^2}}]d(\frac{z}{H}) \tag{2-12}$$

During hot shock, K^0 is defined by $K^0 = \sqrt{\pi H}\bar{E}\bar{\alpha}(T_\infty - T_i)$. The K reaches the maximum

value K_{max} at a specific crack length of $2a^*$ (a^* depends upon the Biot number as shown in Fig.2-2-7)

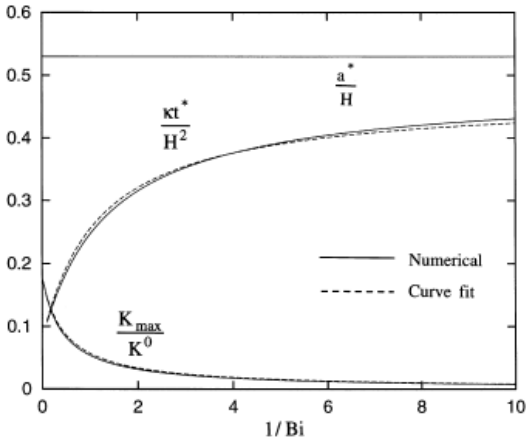

Fig.2-2-7 K_{max} and the corresponding dimensionless values plotted against $1/B_i$. [44].

K is expected to achieve a peak value, $K_{max}= 0.177K^0$, for $B_i = \infty$. After fitting K_{max} with $1/B_i$, the result is approximated by:

$$\bar{K}_{\max} = 0.177(1+\frac{2.12}{Bi})^{-1} \tag{2-13}$$

From Fig.2-2-7, it can be noted that for a full range of Biot numbers, the maximum of K can be reached at a crack length of approximately $a/H = 0.5$.

To rank materials on thermal shock resistance, the maximum temperature jump that the material can sustain, ΔT with $B_i = \infty$. is obtained as:

$$\Delta T = A_4 \frac{K_{IC}}{E\alpha\sqrt{\pi H}} \frac{1}{Bi} \equiv A_4 \frac{K_{IC}}{E\alpha\sqrt{\pi H}} \frac{k}{hH} \tag{2-14}$$

where $A_4 \approx 9.5$ for cold shock and $A_4 \approx 12$ for hot shock.

Increasing specimen size has two detrimental effects on thermal shock resistance. For toughness control failure, it can be seen from the equation that thermal shock resistance decreases as the plate thickness $2H$ increases. Further, when $B_i < \infty$, ΔT decreases with increasing H.

2.3 **Delamination mechanics: energy release rate and stress transient**

Interface delamination is determined to be the major failure mechanism for TBCs deposited by the EB-PVD approach. For delamination that occurs between the ceramic top coat and the metallic bond coat, the two expected failure mechanisms such as the edge delamination and the buckling were compared in Choi and Hutchinson's study [45].

To suppress the edge-delamination, a mode II interface toughness larger than the steady state energy release rate is required. For buckling delamination, a mix mode of interface crack is requisite. During edge delamination, the tip field of a steady state crack is under pure mode II. The related energy release rate is $G_0 = \frac{1-\nu^2}{2E}\sigma_0^2 t$. E and ν represent the Young's modulus and Poisson's ratio of the film and σ_0 is the press stress in the film. During buckle delamination with compressive stress σ_0, the energy release rate along the extension side is given by:

$$G_{side} = G_0(1-\frac{\sigma_c}{\sigma_0})(1+3\frac{\sigma_c}{\sigma_0}) \tag{2-15}$$

where σ_c is the compressive stress required by the described film to buckle along the straight edge.

The energy release rate at the extension front of the buckled area is obtained:

$$\begin{aligned} G_{front} &= G_0(1-\frac{\sigma_c}{\sigma_0})^2 \\ &= G_{side}(1-\frac{\sigma_c}{\sigma_0})(1+3\frac{\sigma_c}{\sigma_0})^{-1} \end{aligned} \tag{2-16}$$

Although the front side of the area experiences a lower energy release rate as shown in Fig.2-3-1, the crack propagates at the delamination front because of the much lower interface fracture toughness.

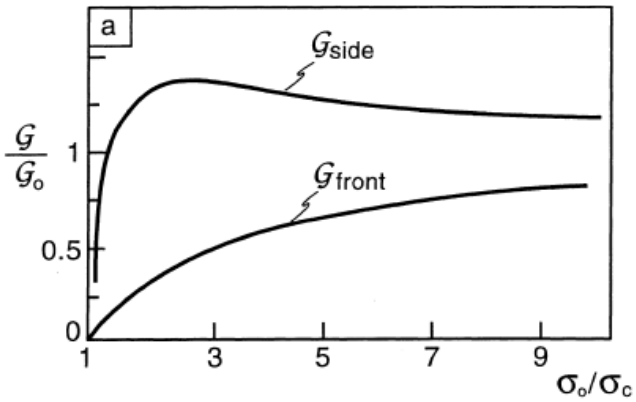

Fig.2-3-1 Energy release rate of the front and side area of a buckling delamination[45].

Phenomena occurring before reaching steady-state decide which of the mechanisms will be dominant. For edge delamination, the size of initial interface flaws is around several layer thicknesses and steady state will be reached with G_0. For buckling delamination, relatively large initial defects are required. Buckling happens when $\sigma_0 / \sigma_c = 1$ and the corresponding half-width b is:

$$\frac{b}{t} = 0.907\sqrt{\frac{E}{(1-\nu^2)\sigma_0}} \tag{2-17}$$

For multilayer films with large delamination conditions,

$$\Delta M = -\int_{y_1}^{y_{f+1}} \Delta\sigma_{xx}(y-c)dy$$
$$\Delta N = \int_{y_1}^{y_{f+1}} \Delta\sigma_{xx}dy \tag{2-18}$$

where ΔM is the bending moment variation about neutral axis and ΔN is the in-plane stress change. Energy release rate at the bond coat and substrate interface is thus:

$$G_{side} = \frac{1}{2S}(N_0 - N_c)(N_0 + 3N_c) \qquad N_c = (\frac{\pi}{b})^2 B$$
$$G_{front} = \frac{N_0^2}{2S}(1-\frac{N_c}{N_0})^2 \qquad N_0 = \sum_{i=1}^{J}\sigma_0^{(i)}t_i \tag{2-19}$$

where S is the stretching stiffness. For small delamination, a similar result is given as:

$$N_c = (\frac{\pi}{b})^2 B + \frac{4k}{\pi^2} E_1^{(3)} b$$

$$G_{side} = \frac{1}{2S}(N_0 - N_c)(N_0 + 3N_c - \frac{16k}{\pi^2} E_1^{(3)} b)$$

$$G_{front} = \frac{1}{b}\int_{b_0}^{b} G_{side} db \qquad (2\text{-}20)$$

where B is the bending stiffness, and b_0 is obtained when N_c is replaced by N_0.

A three-layer system with specific parameters is analyzed for the tendency to buckle. The ratio of in-plane modulus of the layers and initial flaw size are crucial when assessing whether buckling or edge delamination will occur. In addition, a relatively thick top coat will suppress buckling with sufficiently small initial flaw size.

The thermal gradient induced influence on coating delamination behavior has been studied by Evans and Hutchinson [16]. It is argued in their research that delamination within TBC, is dominant by the stress gradient across the coating. Two extreme cool-down paths are investigated. One assumes instantaneous cooling of the surface and a slow uniform cooling afterwards. For the other, the entire system experiences a continuing uniform temperature drop. Delaminations are defined for two different types: (1) Shallow delaminations located in a dense layer formed by coating sintering or calcium-magnesium-aluminosilicate deposits, and (2) Deep delaminations at the interface of top coat and bond coat. The associated critical influential factors for the two types are: the stress gradients induced by transient cooling and the equilibrium temperatures.

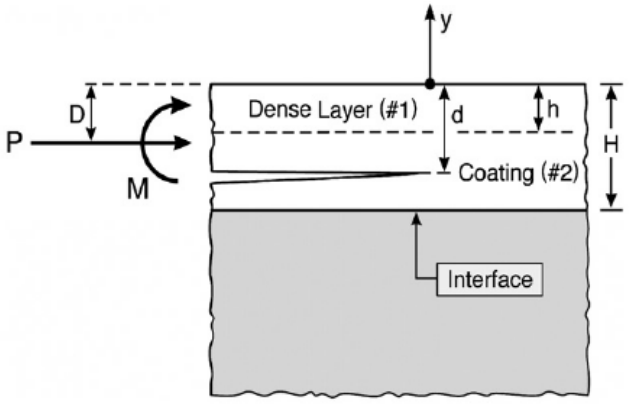

Fig.2-3-2 A schematic of the coating system with dense layer on top [16].

A crack growth criterion is specified in Fig.2-3-2. Delamination parallel to the interface is

assumed. *H* is the coating thickness and *h* is the thickness of the dense layer caused by either deposits ingested into the engine or by sintering of the outermost layer. Conservation of heat flow is ensured, neglecting transient effects caused by thermal diffusivity. Temperature distribution through the coating is decided by thermal conductivities and temperatures of coating surface and substrate at the instant. The distribution of temperature drop which indicates the stresses is obtained as:

$$\Delta T(\eta) = (1 + c_1\eta)\Delta T_{sur/sub} + \Delta T_{substrate} \text{ (in the dense layer)}$$

$$= c_2(1+\eta)\Delta T_{sur/sub} + \Delta T_{substrate} \text{ (in the coating below dense layer)}$$

where

$$c_1 = \frac{k_2 / k_1}{1 - h/H(1 - k_2/k_1)}$$

$$c_2 = \frac{1}{1 - h/H(1 - k_2/k_1)}$$

and $$\eta = y / H \tag{2-21}$$

where *k* is the thermal conductivity of the different layers.

Thus, the stress upon cooling can be written as :

$$\sigma(\eta) = \frac{E_1\alpha_{coating}\Delta T_{sur/sub}}{(1-v_1)}\{1 + c_1\eta - \Phi\} \text{ (in the dense layer)}$$

$$= \frac{E_2\alpha_{coating}\Delta T_{sur/sub}}{(1-v_2)}\{c_2(1+\eta) - \Phi\} \quad \text{(in the coating below dense layer)} \tag{2-22}$$

where Φ is a dimensionless ratio that describes the relationship of mismatch strains between coating layers. The stress gradient is given by:

$$\frac{d\sigma}{dx} = \frac{E_1\alpha_{coating}\Delta T_{sur/sub}}{(1-v_1)H}\frac{k_2/k_1}{1-(h/H)(1-k_2/k_1)} \quad \text{(in the dense layer)}$$

$$= \frac{E_2\alpha_{coating}\Delta T_{sur/sub}}{(1-v_2)H}\frac{1}{1-(h/H)(1-k_2/k_1)} \quad \text{(in the coating below dense layer)} \tag{2-23}$$

For the energy release rate and stress intensity factor, results are presented for

delamination in a homogeneous coating, and the same analysis is for delamination considering dense layer. Defining a force/length and moment/length as:

$$P = \int_{-d}^{0} \sigma(y)dy$$

$$M = \int_{-d}^{0} \sigma(y)(D+y)dy$$

$$K_I = \frac{1}{\sqrt{2}}[Pd^{-1/2}\cos\omega + 2\sqrt{3}Md^{-3/2}\sin\omega]$$
$$K_{II} = \frac{1}{\sqrt{2}}[Pd^{-1/2}\sin\omega - 2\sqrt{3}Md^{-3/2}\cos\omega] \quad (2\text{-}24)$$

Only stress above the delamination plane is taken into consideration.

For the homogeneous layer, $G = \frac{1}{E}(K_I^2 + K_{II}^2) = \frac{1}{2\bar{E}}(\frac{P^2}{d} + 12\frac{M^2}{d^3})$, while (2-25)

for the delamination in a bilayer, $G = \frac{1}{2\bar{E}_2}(\frac{P^2}{Ah} + \frac{M^2}{Ih^3})$, (2-26)

where *A* and *I* are nondimensional parameters related to the equivalent section as illustrated above in another study.

For coating under equilibrium temperature distributions, various conditions are compared. For a shallow delamination with the delamination location of $d/H < 1$, subjected to the mode I conditions, the results are:

$$K_I = \frac{Pd^{-1/2}}{\sqrt{2}\cos\omega} = 1.15Pd^{-1/2}, \qquad G = \frac{K_I^2}{\bar{E}_2} = 1.325\frac{P^2 d}{\bar{E}_2} \quad (2\text{-}27)$$

For a deep interface delamination ($d = H$), the result is:

$$\frac{G}{[(1+\nu_2)/(1-\nu_2)]E_2 H(\alpha_{coating}\Delta T_{sur/sub})^2} = \frac{(1-3\Phi+3\Phi^2)}{6} \quad (2\text{-}28)$$

It is found that, for a deep delamination, the crack experiences pure mode I condition at a certain instant for all locations. The corresponding stress intensity factor and energy release rate are given as:

$$K_I = 0.190\frac{E\alpha\Delta T_{sur/sub}\sqrt{d}}{(1-\nu)},$$
$$\frac{G}{[(1+\nu_2)/(1-\nu_2)]EH(\alpha_{coating}\Delta T_{surf/sub})} = 0.036d/H \tag{2-29}$$

For the case with shallow delaminations, the energy release rate displays a much larger value than that of equilibrium temperature distribution which affirms that shallow delaminations tend to occur upon thermal transient.

The mechanism maps to assess whether delamination will emerge or propagate are given for both shallow and deep delaminations. Several cooling scenarios are analyzed for delamination tendency, as shown in Fig. 2-3-3.

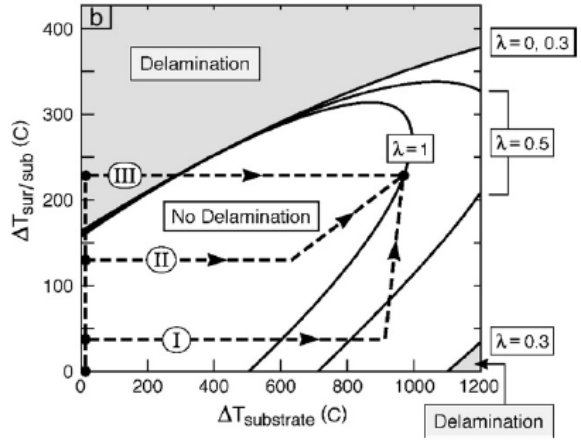

Fig.2-3-3 Delamination map with cooling trajectories for homogeneous coating upon equilibrium cooling [6].

According to the delamination maps, cooling paths that pass through the delamination zone will cause delamination and should be avoided during practical operation of the engine. This kind of maps specifies delamination conditions for different equilibrium cooling scenarios. However, to convert the results into thermal scenarios in practice and further validate the mechanics, more experiments should be carried out to better specify the temperature experience in the coating of the engine.

2.4 **Cyclic Oxidation**

High temperature oxidation causes material failure in land and air based turbines, leading to both property damage and security hazard. Alloys form protective oxide layers under high

temperature environments to pretect materials from further corrosion. However, cracks and then spallation can cause exposure of bare metals. Among all application conditions, cyclic oxidation is one of the most important failure modes of alloys and coatings at high temperatures. Protective thermal coatings provide oxidation resistance to optimize properties in such conditions. While determination of the lifetime of these materials is highly desirable, it can be time consuming and costly to test the full lifetime for certain temperature range. Therefore, different attempts have been made to simulate the cyclic oxidation behavior and predict lifetime.

There are basically three different processes of oxidation in the alloy:

(1) independent oxidation of individual phases

(2) cooperative oxidation of two or more phases

(3) exclusive oxidation of single phase

To describe the behavior of alloys and coatings in heating and cooling conditions, models are developed to quantify the weight change during oxide growth and spallation, giving curves of several vital characters reflecting material degradation. Basically four models have been employed in describing the iterative process. A schematic representation of the four models is shown in Fig.2-4-1.

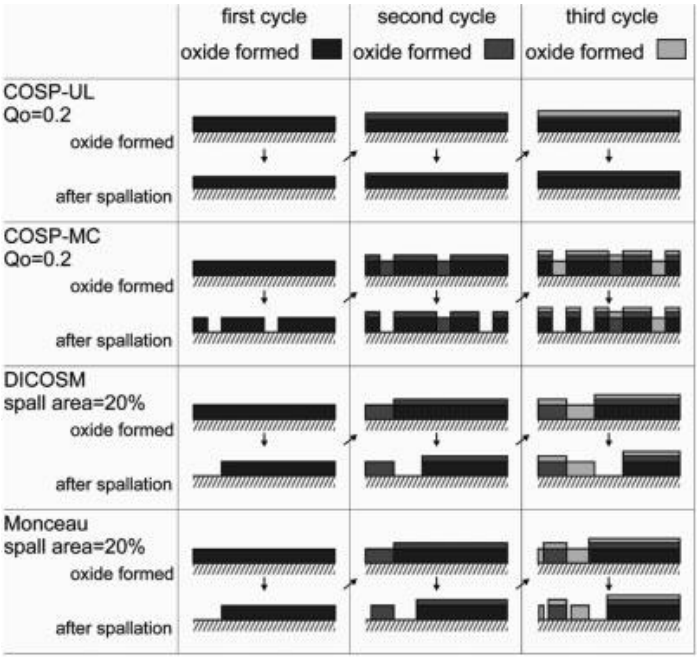

Fig.2-4-1 Schematic of different spallation mechanisms [10].

The basic principle and iterative process of the four models are explained as follows:

The same assumptions are used during heating cycle while cooling mechanism and organization of weight change during cycles vary greatly.

NASA proposed COSP (Cyclic Oxidation Spalling Program), uniform layer model and Random (Monte Carlo) model in 1990. Three assumptions are made:

(1) With constant phase composition, the growth rate of oxide is only a function of oxide thickness.

(2) A monotonic relationship is assumed between spallation and oxide thickness.

(3) The average oxide thickness can be utilized in an approximate random spalling process.

A parabolic law is assumed in the oxide growth stage, providing: $W_{ox} = a \cdot \sqrt{k_p t}$ where W_{ox} is the specific weight of the oxide formation, a is the molecular weight ratio of the oxide to that of oxygen and k_p is the parabolic rate constant. For the following cooling stage, a proportion of oxide will spall as the second assumption described. The oxide spallation fraction F, in the j_{th} cycle is:

$$F = Q_0 \cdot W_{rj} \ ,$$

where Q_0 is called the spall constant, W_{rj} is the total weight of the oxide retained after the jth cycle is completed. Therefore, the weight of spallation is

$$W_{sj} = F \cdot W_{rj}$$

The remaining oxide will then be used to determine the oxide growth of the next cycle. The oxide remained at the end of one circle can thus be obtained. With the amount of the newly formed oxide, the oxide growth and thus the spallation of next cycle can be calculated. In this approach, equivalent time t_{ej} is introduced to attain the total weight of oxide before cooling. t_{ej} is defined as the time required to obtain the same thickness of oxide layer in isothermal conditions as in cyclic oxidation tests. The iterative process of substitution of the above equations will produce the output of oxide formed, spalled and ultimately remained on the alloy.

Comparing the Monte Carlo version of the model with UL model, surface spalls following a different fashion where spallation can occur in random segments and allow full exposure of the metal. The failure from the interface is obviously more severe in practical conditions. This approach numerically divides the surface into a number of separate areas, and for each area, growth and spallation are treated independently. The number of areas, *n*, and the fraction of spallation, *F*,of the area is introduced as new input parameters. Complete spallation takes place when *F* is unity. Distribution of the spallation fraction, *P*, will be set to approximate observed spalling behavior.

Another two models, DICOSM and a statistical model by Monceau [63] assume the surface to spall a constant fraction in each cycle instead of a changing *F* in MC model. For the DICOSM approach, coating surface is divided into a number of segments where exactly one segment spalls during one cycle and interfacial spallation is assumed. The segment to spall is always the one with the thickest oxide. The mechanism is schematically described in Fig.2-4-2. After one cycle, the entire surface grows a scale and one segment with the thickest oxide will spall to the bare metal. The spalled segment is adjacent to the one in the previous cycle only for visual simplicity. According to this model, the weight change for cycle number *j* is obtained:

$j \le n_0$

$$\left(\Delta W / A\right)_A = F_A\sqrt{k_p \Delta t}\left\{\left(2 - S_c\right)\sum_{i=1}^{j}\sqrt{i} + (n_0 - j - 1)\sqrt{j}\right\}$$

$j > n_0$

$$\left(\Delta W / A\right) = F_A\sqrt{k_p \Delta t}\left\{(2 - S_c)\sum_{i=1}^{n_0}\sqrt{i} + \left[\left(1 - S_c\right)\left(j - n_0\right) - 1\right]\sqrt{n_0}\right\} \qquad (2\text{-}30)$$

where F_A is the spall area fraction which equals$1/n_0$, and S_c equals the ratio as mentioned above.

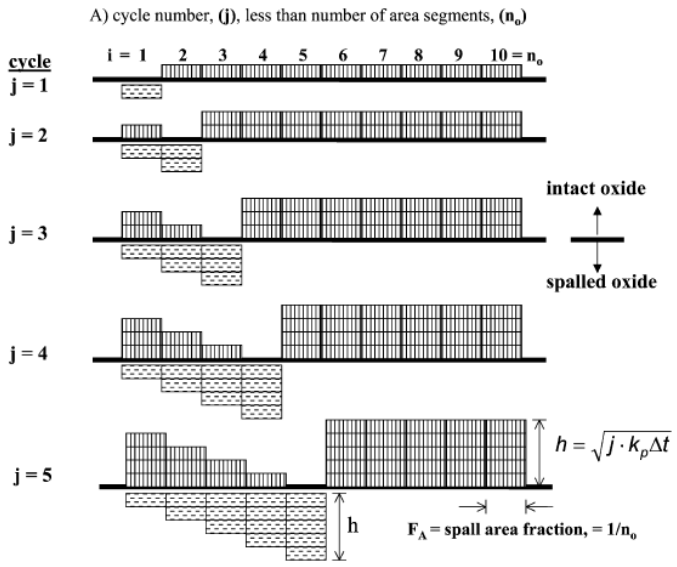

Fig.2-4-2 Schematic cross-section of intact and spalled oxide segments [63].

Although Monceau also assumes constant spallation fraction, segments are organized regarding oxide thickness where the same percentage of spalling occurs in one group.

Efforts based on micromechanics were also made to illustrate failure process. In Chan's work [23], a spallation model based on shear cracks in the oxide layer is developed to represent both the bulk spallation and interfacial spallation. A number of shear cracks are assumed to pre-exist in the coating. To determine the amount of spallation, normalized crack density , ξ, is introduced as: $\xi = \frac{n_c a l_0^2}{BHb}$, where $2a$ is the average length of the shear cracks, l_0 is the initial crack depth, n_c is the number of shear cracks about to form spallation (by developing wing tips), H and B are the height and width of the substrate respectively, and b is the coating thickness. One of the most important characters in this section m is determined by crack density and oxide volume, described by:

$$\xi = \xi_0 \left(\frac{V}{V_0} \right)^m \tag{2-31}$$

The equation is based on the relationship between crack density and oxide volume, where ξ_0 is the crack density at the reference volume, V_0 is the reference volume.

The oxide is subjected to a compressive stress σ_c, with σ_∞ being the applied stress:

$$\sigma_c = E_{ox}\Delta\alpha\Delta T + \sigma_\infty \tag{2-32}$$

The weight of spalled oxide is solved as:

$$W_s = \frac{\xi l_0 \sin^2 2\xi \sin^3 \psi}{\pi K_{ox}^2}\left(E_{ox}\Delta\alpha\Delta T + \sigma_\infty\right)^2 W_{ox} \tag{2-33}$$

Another main parameter, the spallation constant *q*, is defined in the relationship of equivalent time:

$$t_{en} = [t_{e(n-1)} + \tau][1 - q\Delta T^2 W_{ox}] \tag{2-34}$$

Equivalent time is the corresponding time required to form an oxide layer of the identical thickness under isothermal conditions. To evaluate *q* and *m* from experimental data, the equations are given as:

$$W_s = q\Delta T^2 \left[\frac{W_{ox}}{W_0}\right]^{1+m} \tag{2-35a}$$

$$q = \frac{\xi_0 W_0 \sin^2 2\psi \sin^3 \psi}{\pi}\left[\frac{E_{ox}\Delta\alpha\sqrt{l_0}}{K_{ox}}\right]^2 \tag{2-35b}$$

This shed a light on a new aspect to investigate cyclic oxidation behavior. From a more in-depth start point, it makes the approach to simulate high temperature behavior more accurate and convincing.

However, values for ξ_0 and Ψ are difficult to obtain. Although equations based on weight change curve are given, it does not show acceptable applicability in different alloys and temperatures. *q* is adjusted to get better agreement between experimental data and calculated curve. In addition, their physical significance remains an unsolved problem and to get the value from experimental data is of great difficulty.

In addition, all models mentioned above require a “complete” weight change curve as the base to obtain necessary parameters for prediction. In this thesis, effort is made towards finding a new approach to achieve satisfying agreement between experimental and the calculated results and at the same time using less time of the experiments. Therefore, it will become possible to acquire all information needed with the shortest time and least cost which is

important in industrial applications.

The effect on growth rate and spallation output of different parameters has been investigated thoroughly. With increasing S_c, the curve of specific weight change goes down more quickly. A greater value of F_A brings the same effect on the trend [23].

2.5 **Other Studies**

(1) The propagation of a pre-existing edge crack across a finite plate subjected to cold shock

This is studied by Zhao and Lu [47]. For the opposing face, three different types of heat transfer boundary conditions are considered. The mode I crack has three possible modes of growth: extension in plane strain, channeling and spalling. As shown in Fig.2-5-1, the crack may propagate along the thickness of the plate (a), it may channel in the plane of the plate (b), or spall parallel to the surface (c).

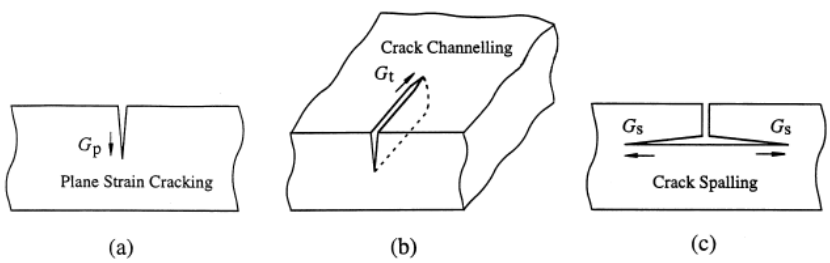

Fig.2-5-1 Three different failure modes in cold shock (a) plane strain cracking (b) channeling (c) spalling [47].

A infinitely large plate with a thickness $2H$ and uniform initial temperature T_i is considered. Coordinates are as depicted in Fig. 2-5-2. For three boundary conditions: (a) an identical cold shock to the top surface, (b) thermal insulation, and (c) constant temperature equal to T_i.

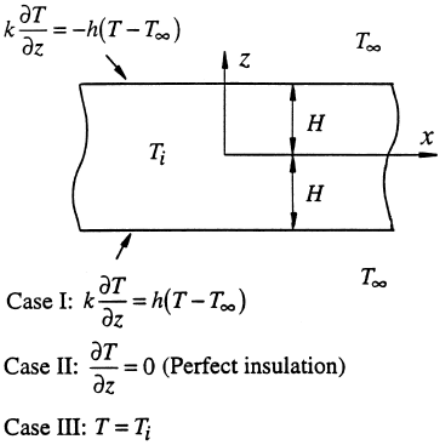

Fig.2-5-2 A plate (no pre-existing crack)subjected to three different boundary conditions [47].

The transient temperature distribution is

$$\frac{\partial^2 T(z,t)}{\partial z^2} = \frac{1}{\kappa}\frac{\partial T(z,t)}{\partial t}, |z| \le H \tag{2-36}$$

With the illustrated initial and boundary conditions, the equation can be solved. For Case I, the temperature field is found to be (Case II and III omitted):

$$\bar{T}(z,t) \equiv \frac{T(z,t) - T_i}{T_i - T_\infty} = -1 + 2\sum_{n=1}^{\infty} \frac{\sin\beta_n \cos(\beta_n z / H)}{\beta_n + \sin\beta_n \cos\beta_n} \exp(-\beta_n^2 \frac{\kappa t}{H^2}) \tag{2-37}$$

β_n are the positive roots of $\beta\tan\beta = B_i$ ($B_i = 10$)

The transient thermal stress distribution in the plate is therefore determined as follows:

$$\bar{\sigma}(z,t) \equiv \frac{\sigma_{xx}(z,t)}{\bar{E}\bar{\alpha}(T_i - T_\infty)} = -\frac{T - T_i}{T_i - T_\infty} + \frac{1}{2H}\int_{-H}^{H} \frac{T - T_i}{T_i - T_\infty} dz + \frac{3z}{2H^3}\int_{-H}^{H} \frac{T - T_i}{T_i - T_\infty} dz$$

$$\bar{\sigma}(z,t) = -2\sum_{n=1}^{\infty} \frac{\sin\beta_n}{\beta_n + \sin\beta_n \cos\beta_n} \{\cos(\beta_n \frac{z}{H}) - \frac{\sin\beta_n}{\beta_n}\} \exp(-\beta_n^2 \frac{\kappa t}{H^2}) \tag{2-38}$$

where

$$\begin{aligned} \bar{E} &= E / (-\nu^2) \\ \bar{\alpha} &= \alpha(+\nu) \end{aligned} \tag{2-39}$$

Under any one of the three conditions, the maximum tensile stress attained at the plate surface increases with increasing Biot number, *B*. Formulas of σ_{max} and t_{max} of the three cases are also given. Emphasis is placed on finding the energy release rate maximized in regard to crack length and time as a function of Biot number. To make solutions valid, short crack

solutions are used. For an edge crack propagating under plane strain condition, the energy release rate G_p at the crack tip is given by:

$$G_p = \frac{K_I^2}{\bar{E}} \tag{2-40}$$

The normalized energy release rate predicted is plotted against crack lengths $\bar{a} \equiv a / H$ for selected dimensionless time $\bar{t} \equiv \kappa t / H^2$ in Fig.2-5-3. It can be noticed that G_p reaches a peak value for all different crack length at a same time of $t \approx 0.1$. The overall maximum of G_p is obtained at $t \approx 0.1$ and $a \approx 0.25$ and the results are similar for Case II and Case III.

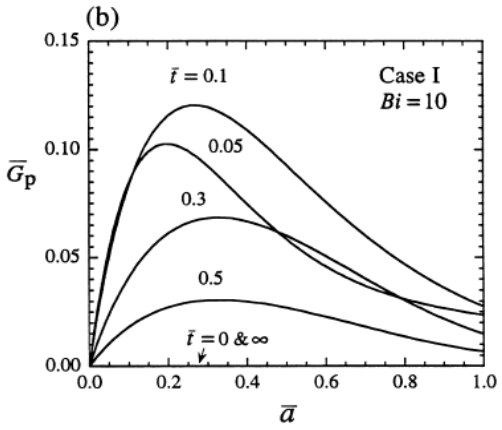

Fig.2-5-3 energy release rate G_p against crack size and elapsed time for plane strain cracking [47].

A failure map (Fig.2-5-4) can be used to determine the failure mode that is the most lilkely to occur when a material with pre-existing cracks is subjected to cold shock. Fig.2-5-4 implies that plain strain cracking tends to dominate when the flaw size, *a*, is relatively small while crack channeling and spalling has a higher tendency for large *a*.

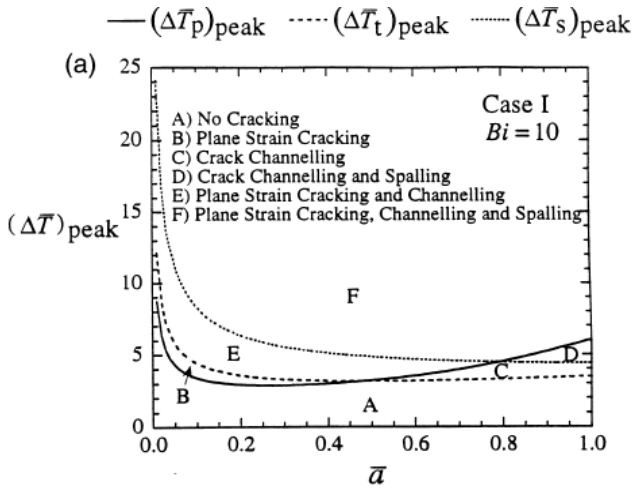

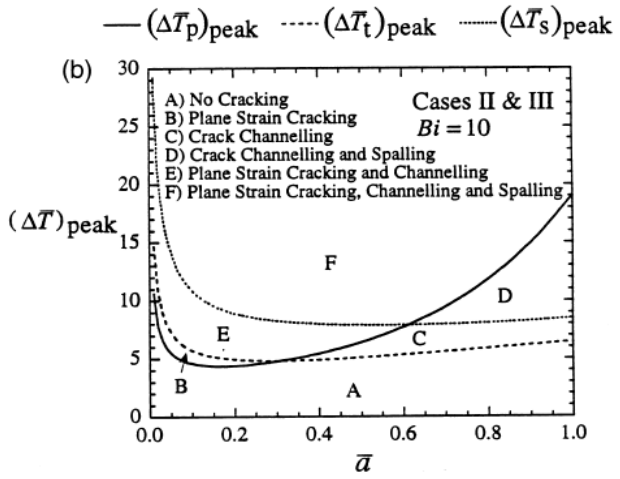

Fig.2-5-4 Failure map for plane strain cracking, channeling and spalling, with B_i = 10 (a) Case I, and (b) Case II and III [47].

(2)Performance examination of silicate deposits in thermal barrier coating with temperature gradients

In the associated experiment, the surface temperature was approximately 1300℃ and the surface is heated at a rate of 110℃/min and the bottom of the substrate is heated at 90℃/min. The coating is deposited by EB-PVD and the two silicate compositions used are $C_{33}M_9A_{13}S_{45}$ and $C_{13}F_{10}A_{18}S_{59}$. The penetration depth through the TBC of the silicate melt is strongly influenced by the temperature gradient since, when temperature decreases, the viscosity of the melt is increased dramatically. The melt viscosity across the coating is given as:

$$\eta(h) = \eta_0 \exp[\beta(\frac{-\Delta T_{TBC}}{H_{TBC}})h + T_{Surf}] \tag{2-41}$$

where *h* is the location measured from the surface, and the penetration velocity is expressed as:

$$\frac{dh}{dt} = \frac{32r}{k_t}\frac{\omega}{(\omega-1)^2}\frac{\sigma_{LV}\cos(\theta)}{\eta(h)h} \tag{2-42}$$

where σ_{LV} is the surface tension of the melt and $cos(\theta)$ is the angle between the melt and the coating, *r* is a hydraulic radius, *w* is the porosity and *k* is a tortuosity factor.

The effect of the silicate on coating stiffness and the thermal expansion coefficient is estimated for an EB-PVD system. The effective modulus of the TBC experiences a dramatic rise when the coating is penetrated by a silicate melt. However, when TBC has less than 20% porosity and the second phase was to crystallize from a silicate glass, the modulus will not change significantly. The magnitude of the compressive stress and thus the energy release rate increases as the penetration depth increases. *G* is obtained by:

$$G = U[\xi_0, \kappa] - (U^t[\xi_0^t, \kappa^t] + U^b[\xi_0^b, \kappa^b]) \tag{2-43}$$

where the strain energy U_i in different layer is defined by：

$$U_i = \int_{y_b^i}^{y_t^i} [\frac{1+\nu}{2E}(\sigma_x^2 + \sigma_z^2) - \frac{\nu}{2E}(\sigma_x + \sigma_z)^2] dy \tag{2-44}$$

where y_t^i and y_b^i define the top and bottom of the layer *i.*

CHAPTER 3. TBC DELAMINATION IN THERMAL GRADIENTS

3.1 Methodology

In this chapter, two models of TBC delamination in a thermal gradient are combined: the first one mostly focuses on the stress distribution in TGO with undulated interface and the second one analyzes a coating's incidence of delamination with different locations under several cooling trajectories. The goal of this part of this chapter is to mitigate delamination to extend coating lifetime and enhance coating reliance.

To develop the mechanics systematically, the research is organized in the following manner:

(1) Plots relating temperature differences are used to obtain energy release rate of coating under thermal gradient conditions.

(2) A spherical model is used in combination with an existing layer system to identify the coatings with TGO formation. The coating interface is modified as undulated. General results for energy release rate due to thermal mismatch and TGO growth are derived.

(3) Results for energy release rates from both (1) and (2) are applied to develop delamination maps and analyze different cooling scenarios.

When experiencing rapid cooling down of the system, either from back-side cooling or from engine shut down, a large thermal gradient is induced [32].The thermal gradient causes strain in constituents among coatings [16] [25].Observation has indicated that coatings are more susceptible to delaminations under this condition [30]. Delaminations are predominantly located:

(1) within the top coat, referred as shallow delamination, and

(2) at the interface of TBC and bond coat (TGO not considered), referred as deep delamination

In this section, a modification of an existing model is proposed to better explain the delamination mechanism and analyze the influence of cool-down history to delamination.

To analyze the delamination, a crack growth criterion is specified. A bilayer system with crack parallel to the surface has been proposed, as shown in Fig.3-1-1.

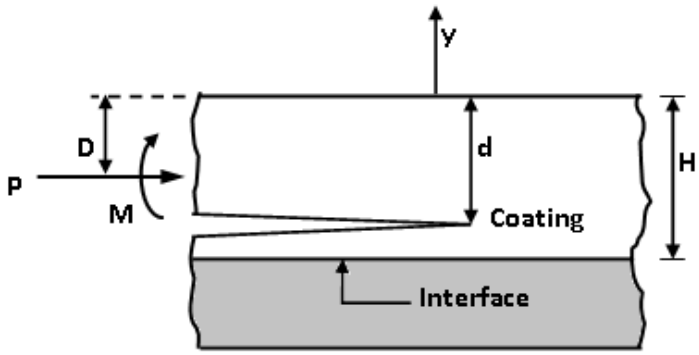

Fig.3-1-1 A schematic of the coating system presented.

Here, P and M are force/length and moment/length defined over the delamination plane respectively, and D is the location of the neutral bending axis.

The top coat thickness is denoted as H and the crack is asusumed to appear at the depth d into the coating and is parallel to the free surface, the model is analyzed and discussed under following assumptions [16]:

(1) As engine power is reduced, the temperature of the coating surface is instantly reduced to the air temperature, and the coating and substrate then cool down uniformly.

(2) The dense layer caused either by calcium-magnesium-aluminosilicate deposits or sintering of outmost TBC are neglected, and the thermal gradient induced stress is the main concern in this section.

(3) Each layer of the system is homogeneous.

The material properties such as Young's modulus and strength may vary during the cooling process, such variations are neglected in this study. All mechanical property coefficients of the system are assumed to be unaffected upon cooling.

The initial temperature of the coating surface and substrate are denoted as $T^i_{surface}, T^i_{substrate}$ respectively. The corresponding parameters for Young's modulus, Poisson's ratio, thermal

conductivity of the coating and substrate are respectively denoted as $E_{tbc}, \upsilon_{tbc}, \kappa_{tbc}, E_{sub}, \upsilon_{sub}, \kappa_{sub}$. $\Delta\alpha$ is set to be $\Delta\alpha = \alpha_{sub} - \alpha_{tbc}$, i.e.,the difference between top coat and substrate thermal expansion coefficient. The temperature quantity, $\Delta T_{sur/sub}$ is denoted by.

$$\Delta T_{sur/sub} = \Delta T_{surface} - \Delta T_{substrate} \tag{3-1}$$

Since the biaxial in-plane stress is contributed by one factor proportional to $\alpha_{coating}\Delta T_{sur/sub}$ and another proportional to $\Delta\alpha\Delta T_{substrate}$, the stress in the coating during cooling down can be expressed as:

$$\sigma(\eta) = \frac{E_{tbc}\alpha_{tbc}\Delta T_{sur/sub}}{(1-\upsilon_{tbc})}\left[\frac{1-\eta}{k_2/k_1} - \Phi\right] \tag{3-2}$$

where η is y/H, y is the distance from the surface (negative in value),and Φ is the dimensionless ratio of mismatch strains, obtained by:

$$\Phi = \frac{\Delta\alpha\Delta T_{sub}}{\alpha_{tbc}\Delta T_{sur/sub}} \tag{3-3}$$

Φ is also described as the “cooling parameter” when analyzing the influence of cooling path to delamination mechanism.

The stress gradient is given by:

$$\frac{d\sigma}{dy} = \frac{E_{tbc}\Delta T_{sur/sub}}{(1-\upsilon_{tbc})H} \tag{3-4}$$

It is known that the rate of stress change is a critical factor when considering coating failure during cooling process. The expression indicates that the difference between surface temperature drop and substrate temperature change is the key factor towards stress gradient.

In the homogeneous coating with equilibrium temperature distribution, the stress distribution is linear through the coating [16]:

$$\sigma = \bar{\sigma} + \sigma_0(1+2\eta)$$

where $\bar{\sigma} = E_{tbc}\alpha_{tbc}\Delta T_{sur/sub}(1/2-\Phi)/(1-\upsilon_{tbc})$, and

$$\sigma_0 = \left[E_{tbc}\alpha_{tbc}\Delta T_{sur/sub} / 2\left(1-\nu_{tbc}\right)\right] \tag{3-5}$$

The largest instantaneous temperature drop without causing delamination, referred as temperature allowance, for both delamination locations is necessary for accessing the reliability of coating performance.

3.2 Bi-layer system

Results have been presented for stress intensity factors and energy release rates of homogeneous coatings under thermal gradient conditions. As *y* being the coordinate in Fig.3-1-1, starting from the coating surface, *σ(y)* is the stress distribution of in-plane stress. The force/length and moment/length are defined over the delamination plane:

$$\begin{aligned} P &= \int_{-d}^{0} \sigma\left(y\right) dy \\ M &= \int_{-d}^{0} \sigma\left(y\right)\left(D+y\right) dy \end{aligned} \tag{3-6}$$

where *D* is the location of the neutral bending axis, taken as the depth of *d*/2 below the surface. By substituting the equation of stress, the expression of *P* and *M* are obtained as follows:

$$\begin{aligned} P &= \left(\bar{\sigma}+\sigma_0\right)d - \sigma_0 d^2 / H \\ M &= \sigma_0 d^3 / \left(6H\right) \end{aligned} \tag{3-7}$$

For a delamination located at depth *d*, assuming in an infinite deep and homogeneous layer, the stress intensity factor and energy release rate are derived as:

$$\begin{aligned} K_I &= \frac{1}{\sqrt{2}}\left[Pd^{-1/2}\cos\omega + 2\sqrt{3}Md^{-3/2}\sin\omega \right] \\ &= \frac{P}{\sqrt{2Ah}}\cos\omega + \frac{M}{\sqrt{2Ih^3}}\sin\omega \\ K_{II} &= \frac{1}{\sqrt{2}}\left[Pd^{-1/2}\sin\omega - 2\sqrt{3}Md^{-3/2}\cos\omega \right] \\ &= \frac{P}{\sqrt{2Ah}}\sin\omega - \frac{M}{\sqrt{2Ih^3}}\cos\omega \end{aligned} \tag{3-8}$$

$$G = \frac{1}{\bar{E}}\left(K_I^2 + K_{II}^2\right) = \frac{1}{2\bar{E}}\left(\frac{P^2}{d} + 12\frac{M^2}{d^3}\right) \tag{3-9}$$

where $\bar{E} = E/\left(1-\upsilon^2\right)$ and $\omega = 52.1^\circ$ [33][35]. The results above are the base for the analysis ensued, which is applicable for different crack location situations and stress distributions. For deep delamination where delamination occurs at the interface between coating and substrate, non-dimensional quantities *A* and *I* in equation (3-8) are calculated to be 1 and 1/12.

Research has discovered that for deep delamination to generate at the interface, it can extend in a mixed mode while shallow delamination between surface and substrate extend in pure mode I. The expression used to characterize the fracture toughness depending on mode mix is:

$$\Gamma_C^i = \Gamma_{IC}^i\left[1 + \tan^2\left(\left(1-\lambda\right)\psi\right)\right] \tag{3-10}$$

where Γ_{IC}^i is the mode I toughness and Ψ is the phase angle, presented in terms of the stress intensity factor, and parameter λ describes the mode mix.λ varies from 0 to1.0.

3.2.1 Case I. Stress intensity factor and energy release rates for deep delamination

For delamination at the interface of coating and substrate, the result of energy release rate under equilibrium temperature distribution is given as:

$$G = \frac{H}{6\bar{E}}\left(3\sigma^2 + \sigma_0^2\right) \tag{3-11}$$

The critical requirement of coating delamination can be given by the fact that a crack will propagate only when the energy that the material releases after the fracture equals or exceeds the energy that it can absorb before fracture. Therefore, by imposing $G = \Gamma_C^i$, and considering equation (3-4), the delamination map can be defined by the boundaries obtained from:

$$Y^2 - 3XY + 3X^2 = 6\left[1 + \tan^2\left(\left(1-\lambda\right)\psi\right)\right] \tag{3-12}$$

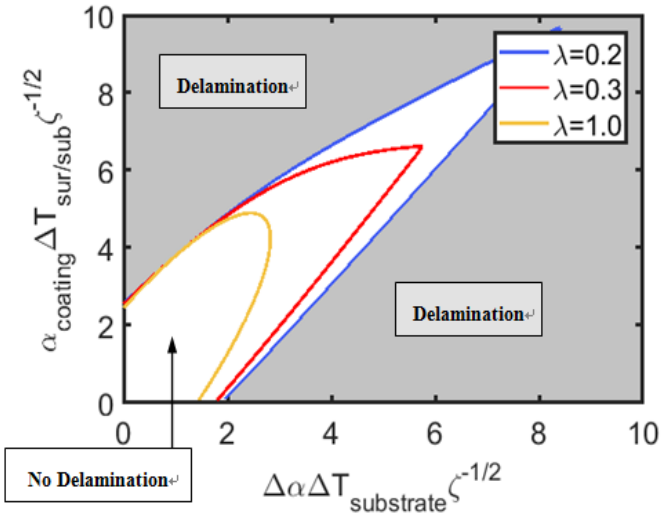

Fig.3-2-1 Delamination map of homogeneous coating for equilibrium cooling (dimensionless boundaries).

The criteria used here is $G=\Gamma_C^i$, the delamination will propagate only when the energy release rate exceeds the fracture toughness from equation (3-4).

$$X=\Delta\alpha\Delta T_{sub}\varsigma^{-1/2}, Y=\alpha_{tbc}\Delta T_{sur/sub}\varsigma^{-1/2} \tag{3-13}$$

$$\varsigma=\left[\frac{(1-\nu)}{(1+\nu)}\frac{\Gamma_{IC}^i}{EH}\right] \tag{3-14}$$

By generating plots using, $x=\Delta T_{sub}$, i.e., temperature drop at the substrate, and $y=\Delta T_{sur}$, i.e., temperature drop at the coating surface, the corresponding energy releaserate can be written as:

$$G=1-\frac{3\Delta\alpha}{\alpha_{tbc}\left(\frac{y}{x}-1\right)}+3\left(\frac{\Delta\alpha}{\alpha_{tbc}\left(\frac{y}{x}-1\right)}\right)^2\frac{1+\nu}{1-\nu}\cdot EH\alpha_{tbc}^2(y-x) \tag{3-15}$$

Defining a new dimensionless ratio of mismatch strain: $\Phi'=\frac{y}{x}=\frac{\Delta T_{surface}}{\Delta T_{substrate}}$, by imposing equations (3-15) and (3-10),a new delamination boundary is obtained:

$$\left[\alpha_{tbc}^2y^2+xy\left(-2\alpha_{tbc}^2-3\Delta\alpha\alpha_{tbc}\right)+x^2\left(\alpha_{tbc}^2+3\Delta\alpha\alpha_{tbc}+3\Delta\alpha^2\right)\right]\zeta^{-1}=6\left\{1+\tan^2\left[(1-\lambda)\psi\right]\right\} \tag{3-16}$$

The results from the equation above are plotted in Fig.3-2-2 for several λ values. For λ=1,

the toughness is mode independent, while as λ decreases, the toughness dependence on mode becomes stronger.

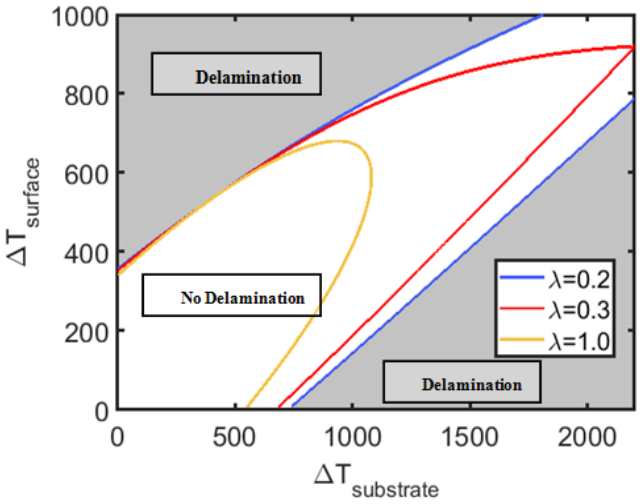

Fig.3-2-2 Delamination map for coating with different mode mix

All parameters and constants implicated are listed in Table. I.

Table. I Summary of material properties used for calculation

1.TBC	
Thermal expansion coefficient (1/K), α_{tbc}	1.1×10^{-5}
Young's modulus,E_{tbc}	$43GPa$
Poisson's ratio,ν_{tbc}	0.2
Coating thickness, H	$2.5\times10^{-4}(m)$
Mode I toughness,Γ_{IC}^{i}	$38\left(J/m^2\right)$
2.TGO(α-Al_2O_3)	
Thermal expansion coefficient, α_o	$8-9\times10^{-6}$
TGO thickness, h	$1-6\times10^{-6}(m)$
3.Bond coat	
Thermal expansion coefficient (1/K), α_s	1.3×10^{-5}

Ratio of TGO vs consumed bcvolume,*m*	1.3
Imperfection radius,*R*	$2\times10^{-5}(m)$
Substrate	
Thermal expansion coefficient (1/K), α_{sub}	1.5×10^{-5}

3.2.2 Case II. Shallow delamination

For shallower delamination located between the surface and interface (*d*<*H*), research indicates that it is subjected to pure mode I conditions, and follows a relationship,

$$d / H = 1.38(1-\Phi) \tag{3-17}$$

where *d* is the depth of crack and *H* is the coating thickness.

It can be concluded that a pure mode I shallow crack can only form and propagate with sufficient temperature drop. Equation (3-11) indicates that for a shallower delamination (*d/H*≈0.1), due to the small value of energy release rate, the formation can be excluded under equilibrium temperature conditions. The relevant condition for mode I crack to propagate is $0.275<\Phi<1$.

By substituting equation (3-17) into (3-11), the energy release rate is derived to be:

$$G = 0.176(1-\Phi)^3\left(\frac{1+\nu}{1-\nu}\right)E_{tbc}H\left(\alpha_{tbc}\Delta T_{sur/sub}\right)^2 \tag{3-18}$$

With the same approach illustrated in the case I, the boundaries can be obtained as:

$$Y^2-3XY+3X^2-X^3/Y=1/0.176 \tag{3-19}$$

with the new coordinates: $x=\Delta T_{substrate}, y=\Delta T_{surface}$,

$$G = 0.176E_{tbc}H\alpha_{tbc}^2\left(\frac{1+\nu}{1-\nu}\right)\frac{\left[y-\left(\frac{\alpha_{sub}}{\alpha_{tbc}}\right)x\right]^3}{y-x} \tag{3-20}$$

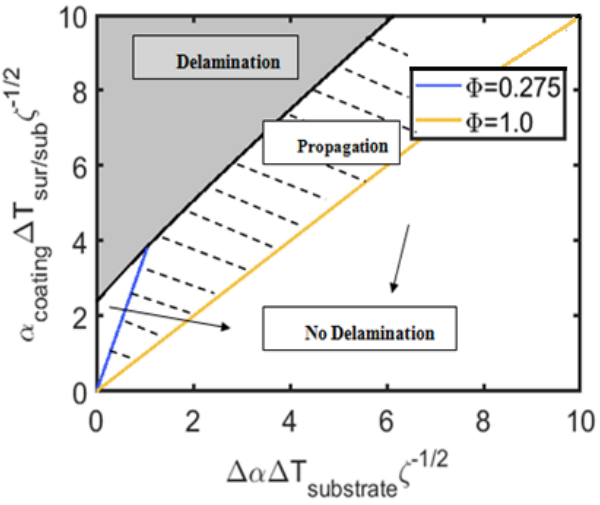

Fig.3-2-3 Mechanism map for homogeneous coating under shallow delamination with dimensionless boundaries.

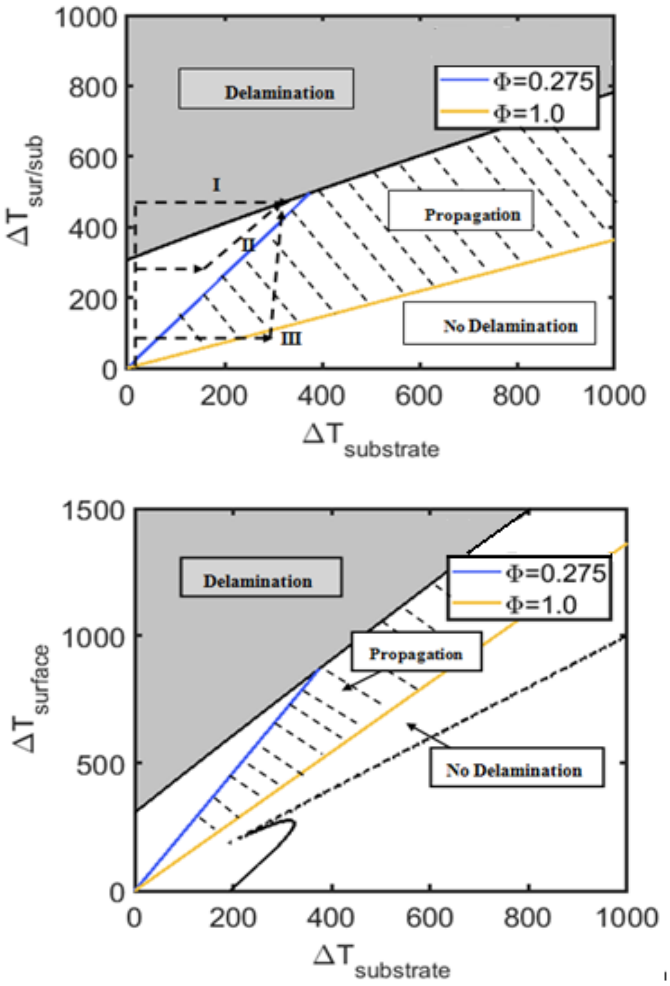

Fig.3-2-4 Mechanism map for homogeneous coating under shallow delamination with temperature drop boundaries.

The corresponding mechanism maps for shallow delamination are shown in Fig.3-2-3 and Fig.3-2-4.

Besides the boundaries determined by energy release rate, the other two straight boundaries are provided by the condition $0.275 < \Phi < 1$, which is defined by the assumption that the crack will propagate in pure mode I. Therefore, the area for pre-existed pure mode I crack to propagate is set with all the conditions above. Note that in the latter map, the boundaries are not dimensionless, with surface temperature drop represented by *x* and substrate temperature drop represented by the *y* axis.

The maps specify delamination conditions for different equilibrium cooling processes. Three different cooling paths are analyzed for three cooling scenarios to ascertain the actual possibility of delamination. All trajectories begin at the point when the substrate and coating surface are subjected to 900℃ and 1130℃ respectively. Any trajectory that enters the delamination zone during cooling is expected to have delamination in the system. The related trajectories are analyzed only for deep delamination conditions. Briefly, one represents rapid surface temperature drop, one is for slow cooling and one is for balanced surface and substrate cooling. The first one experiences an instantaneous surface cooling, resulting in the system to enter delamination zone. Then it is followed by a uniform cooling of the coating and substrate. Delamination of pure mode I will generate in this trajectory. Trajectory II indicates a smaller surface cooling, followed by uniform cooling of coating and substrate. The process ends with the surface keeping cooling down more rapidly than the substrate. For trajectory II, the cooling path is kept in the delamination free area. No delamination will develope or propagate in this trajectory. Trajectory III indicates a more persistent substrate cooling, which passes through the propagation area and leads to propagating of pre-existed crack. It is obvious that the second trajectory provides the optimal path to avoid delamiantion which has great referential importance in engine operation in practice.

However, the results above are obtained without considering the critical effect caused by TGO. TGO has a huge influence on coating delamination by inducing growth stress, thermal mismatch and also influences stress development over time by creeping. In addition, the

interface of the existing model is considered to be flat which ignores the effect of interface roughness on stress state and fracture toughness. Therefore, the interface is modified to be undulated and a local spherical model is induced to describe the interface. In the following paragraph, the spherical symmetric model with TGO will be introduced into the layer system. The corresponding stress and energy release rate will be derived.

3.3 Spherical symmetric system

3.3.1 TGO induced stress

For EB-PVD fabricated coatings, cracks are mostly found to appear at the interface between TGO and bond coat or within TGO, which indicates that TGO plays an important role in failure mechanism. Under operating temperatures, the TBC is exposed to oxidation of the bond coat. The oxygen ions travel through the ceramic top coat continuously and react with the aluminum in the BC, resulting in the formation and thickening of a thin layer of alumina. It has been found that the failure of the TBC is correlated with TGO thickness. The growth of TGO is dominated by the diffusion of oxygen rather than by the interface [17].

A minimum amount of aluminum is required to form a protective alumina scale, and 6wt.% of aluminum is commonly taken as the critical value for alumina formation. Upon this value being reached, less protective oxide (such as oxides formed with Ni and Cr) will start to appear, leading to a much faster failure of the coating.

The understanding of stress in TGO is vital to any model of TBC system. Two main sources of stress are considered in this section: the stress due to thermal expansion misfit and the other one dur toTGO growth. The main motivation is to evaluate the energy release rate in both TGO and top coat.

During TGO growth, it experiences large compression, especially during coating cooling process. It usually leads to the out of plane displacement and then the buckling of the bond coat. Additionally, it induces tensile stress to the interface and causes delamination [3]. Imperfections have been observed to exist around TGO, at the interface between TBC and BC. Since TGO will extend itself and form an undulated wavy morphology as shown in Fig.3-3-1[19], considering the interface as a plane is imprecise.

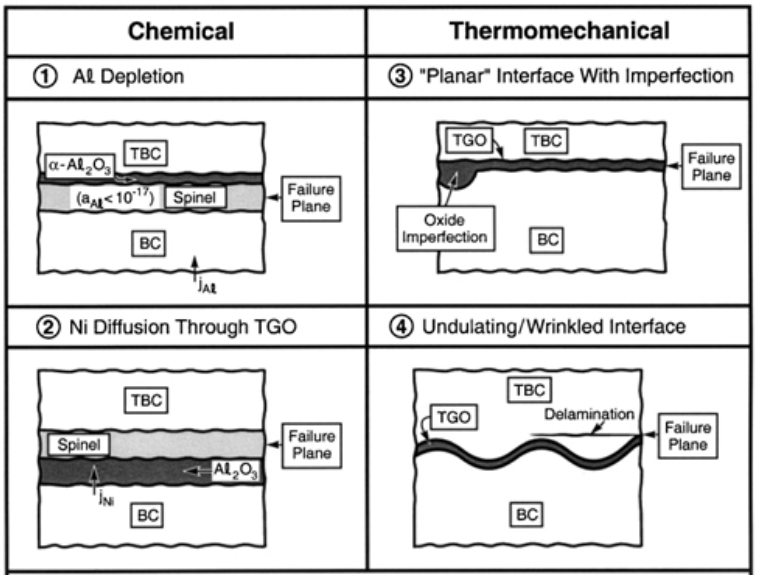

Fig.3-3-1 A schematic of interface morphology change during TGO growth [18].

To better analyze actual stress distribution around the TGO, a spherically symmetric model has been proposed by Karlsson to investigate the stress distribution and solve the model numerically [19].

The schematic of the modified coating system is shown in Fig.3-3-2, where *h* is the TGO thickness, *r* is the distance from the centre of the sphere to the calculated point, 2*R* is the diameter of the imperfection [21].

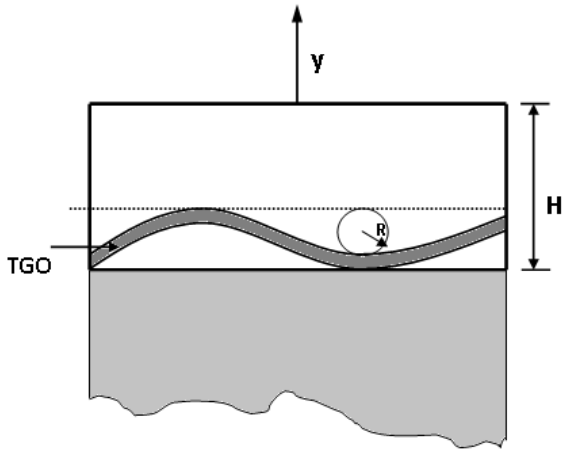

Fig.3-3-2 Schematic of model combining multilayer system and spherical system.

In Evans' work regarding mechanics-based scaling laws for the durability of thermal barrier coatings, a spherically symmetric model of imperfections is presented [21]. TBC TGO and bond coat are assumed to have the same elastic properties including Young's modulus *E*,

and Poisson's ratio *v*. In addition, the relationship of the thermal expansion coefficients of the three materials follows $\alpha_o \le \alpha_{tbc} \le \alpha_{sub}$. Note that the elastic modulus and interface fracture toughness in real case change with exposure time [20]. The stress developed in the spherical imperfection model is illustrated in Fig.3-3-3.

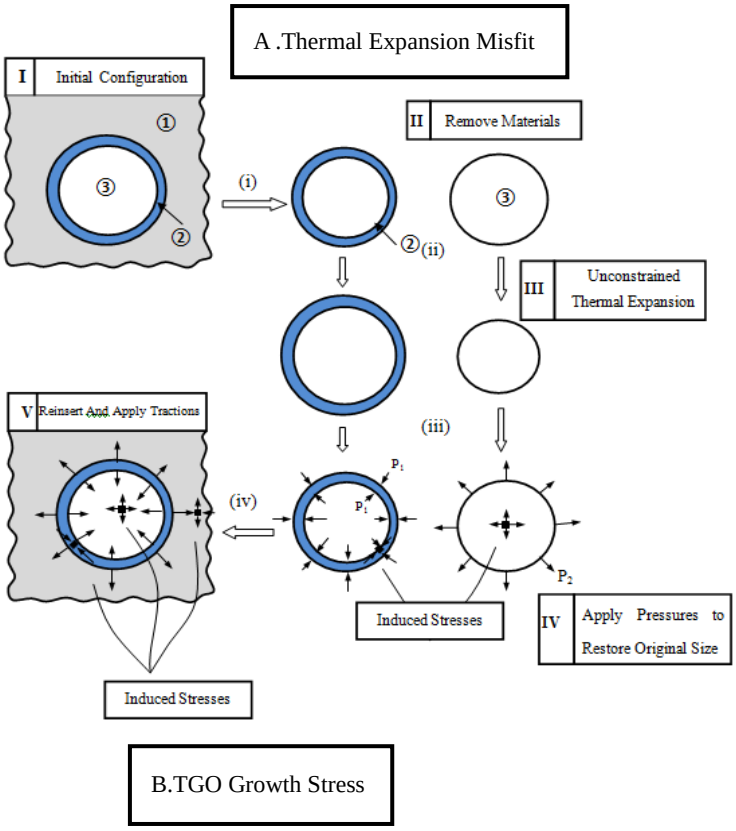

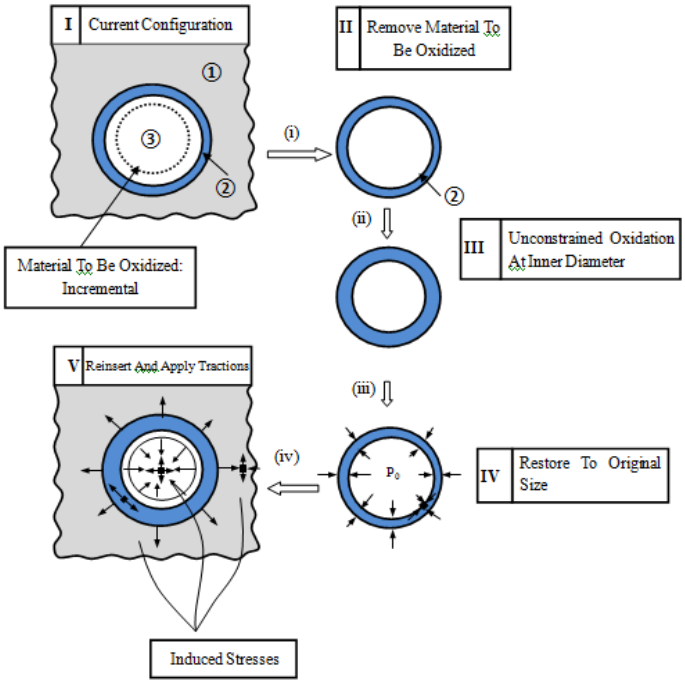

Fig.3-3-3 Stress developed around spherical imperfections for (a) Thermal expansion misfit (b) TGO growth [21].

The solutions for the stress due to thermal expansion misfit in the spherical symmetry have been derived. For the TGO, the meridional stress and the hoop stress are:

$$\sigma_{rr} = \Lambda\{\alpha_{tbc} - \alpha_o - (\alpha_s - \alpha_o)[(R-h)/r]^3\} \tag{3-22}$$

$$\sigma_{\theta\theta} = \Lambda\{\alpha_{\text{tbc}} - \alpha_o + \frac{1}{2}(\alpha_s - \alpha_o)[(R-h)/r]^3\}$$

where $\Lambda = 4\kappa\Delta T/[\kappa + 4\mu/3]$, $\mu = E/[2(1+\upsilon)]$, $\kappa = E/[3(1-2\upsilon)]$, and ΔT is the temperature drop which is negative in sign.

The corresponding stresses in the TBC are:

$$\sigma_{\text{rr}} = -2\sigma_{\theta\theta} = -\Lambda\{\alpha_o - \alpha_{tbc} + (\alpha_s - \alpha_o)(1-h/R)^3\}(R/r)^3 \tag{3-23}$$

By considering that the interface of the TGO and TBC has the shape of an undulated trace, the two models are combined as shown in Fig.3-3-2. Deep delamination (as the case I in the last section) is taken into account in this case. From SEM observation from previous research, the valley of the interface between the ceramic coating and TGO has the biggest tendency to crack. The energy release rates in the TGO and TBC are calculated by applying

the approach described in last section. Only radial stress has an impact on delamination at the valley. By using coordinates based on the spherical nature of imperfections, the moment end load *P* and moment *M* are obtained in this case as:

For *P* and *M* within the TGO:

$$y = -(d - R + r)$$

$$r = -y - d + R$$

$$P = \int_{-d}^{-(d-h)} \sigma(y)dy$$

$$= \int_{-d}^{-(d-h)} \Lambda\{\alpha_{tbc} - \alpha_o - (\alpha_s - \alpha_o)[(R-h)/r]^3\}dy$$

$$= \Lambda h(\alpha_{tbc} - \alpha_o) - (\alpha_s - \alpha_o)(R-h)^3 \int 1/r^3 dy$$

$$= \Lambda h(\alpha_{tbc} - \alpha_o) - (\alpha_s - \alpha_o)(R-h)^3 \cdot \int_{R-h}^{R} (-\frac{1}{r^3})dr$$

$$= \Lambda h(\alpha_{tbc} - \alpha_o) - \frac{1}{2}(\alpha_s - \alpha_o)(R-h)^3 \cdot [\frac{1}{R^2} - \frac{1}{(R-h)^2}] \quad (3\text{-}24)$$

$$M = \int_{-d}^{-(d-h)} \sigma(r)(D+y)dy$$

$$= \frac{1}{2}d \cdot P + \Lambda(\alpha_{tbc} - \alpha_o) \cdot \frac{1}{2}y^2 \Big|_{-d}^{-(d-h)} +$$

$$(\alpha_s - \alpha_o)(R-h)^3 \int_{R-h}^{R} \frac{-d + R - r}{r^3} dr$$

$$= \frac{1}{2}d \cdot P + \frac{\Lambda}{2}(\alpha_{tbc} - \alpha_o)(2dh + h^2) + (\alpha_s - \alpha_o)(R-h)^3 \cdot$$

$$\left[\frac{d+R}{2}\left(\frac{1}{R^2} - \frac{1}{(R-h)^2}\right) + \left(\frac{1}{R} - \frac{1}{R-h}\right)\right] \quad (3\text{-}25)$$

For *P* and *M* within the top coat:

$$
\begin{aligned}
P &= \int \sigma(r)\,dy \\
&= \int_{-(d-h)}^{0} -\Lambda\left\{\alpha_o - \alpha_{tbc} + (\alpha_s - \alpha_o)\left(1-\frac{h}{R}\right)^3\right\}\left(\frac{R}{r}\right)^3 dy \\
&= -\Lambda\left\{\alpha_o - \alpha_{tbc} + (\alpha_s - \alpha_o)(1-h/R)^3\right\} R^3 \int_{R-d}^{R-h} \frac{1}{r^3}\,d(-r) \\
&= \frac{1}{2}\Lambda\left\{\alpha_o - \alpha_{tbc} + (\alpha_s - \alpha_o)(1-h/R)^3\right\} \frac{R^3}{(R-h)^2 - (R-d)^2}
\end{aligned}
\tag{3-26}
$$

$$
\begin{aligned}
M &= \int \sigma(r)(D+y)\,dy \\
&= \frac{1}{2}dP + \int \sigma(r)(-d+R-r)(-dr) \\
&= \frac{1}{2}dP - \Lambda\left\{\alpha_o - \alpha_{tbc} + (\alpha_s - \alpha_o)(1-h/R)^3\right\} R^3 \int \frac{r+d-R}{r^3}\,dr \\
&= \frac{1}{2}dP - \Lambda\left\{\alpha_o - \alpha_{tbc} + (\alpha_s - \alpha_o)(1-h/R)^3\right\} R^3 \left[-r^{-1}\Big|_{R-d}^{R-h} - \frac{1}{2}r^{-2}(d-R)\Big|_{R-d}^{R-h}\right] \\
&= \frac{1}{2}dP - \Lambda\left\{\alpha_o - \alpha_{tbc} + (\alpha_s - \alpha_o)(1-h/R)^3\right\} R^3 \cdot \\
&\left[\left(\frac{1}{R-d} - \frac{1}{R-h}\right) + \frac{d-R}{2}\left(\frac{1}{(R-d)^2} - \frac{1}{(R-h)^2}\right)\right]
\end{aligned}
\tag{3-27}
$$

It can be noted from the equations (3-24), (3-25), (3-26) and (3-27) that both P and M change with Λ, thus they also vary with temperature change, indicating that the corresponding energy release rate changes during the cooling process.

The energy release rate from the above result is obtained with respect to the temperature drop of the coating: G_{TGO} has so little impact that it can be considered neligible; the depedence of G_{TBC} on temperature change is shown in Fig.3-3-4. It is found that, with the changing TGO thickness, the result almost remains constant in contrast with the energy release rate due to CTE mismatch between the top coat and substrate.

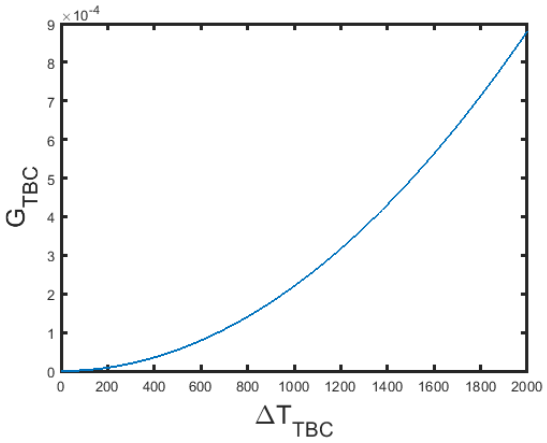

Fig.3-3-4 Energy release rate induced by TGO CTE mismatch over temperature drop.

The TGO growth induced stress is mostly due to the formation of α-alumina at the interface where the bond coat is consumed during oxidation. The stresses, forces, and moments for TGO and TBC are determined as (Note: Creep and plasticity are neglected)

In the TGO：

$$\sigma_{rr} = -\frac{2E(m-1)h}{3(1-\upsilon)mR} \tag{3-28}$$

$$P = \frac{2E(m-1)h^2}{3(1-\upsilon)mR} \tag{3-29}$$

$$\begin{aligned} M &= \int \sigma(r)(D+y)dy \\ &= \frac{1}{2}dP + \frac{2E(m-1)h}{3(1-\upsilon)mR} \cdot \int_{-(d+h)}^{-d} (-d+R-r)dr \\ &= \frac{1}{2}dP - \frac{2E(m-1)h}{3(1-\upsilon)mR} \cdot \left(\frac{1}{2}r^2 + dr - Rr\right)\Big|_{-(d+h)}^{-d} \\ &= \frac{1}{2}dP + \frac{Eh^2(m-1)(2R+h)}{3(1-\upsilon)mR} \end{aligned} \tag{3-30}$$

In the top coat:

$$\sigma_{rr} = -\frac{2E(m-1)hR^2}{3(1-\upsilon)m} \cdot \frac{1}{r^3} \tag{3-31}$$

$$
\begin{aligned}
P &= \int \sigma(r)\,dy \\
&= -\frac{2E(m-1)hR^2}{3(1-\upsilon)m} \cdot \int_{R-d}^{R-h} \frac{1}{r^3}\,dr \\
&= \frac{2E(m-1)hR^2}{3(1-\upsilon)m} \cdot \left(-\frac{1}{2} r^{-2} \right) \Big|_{R-d}^{R-h} \\
&= \frac{E(m-1)hR^2}{3(1-\upsilon)m} \cdot \left[\frac{1}{(R-d)^2} - \frac{1}{(R-h)^2} \right]
\end{aligned} \tag{3-32}
$$

$$
\begin{aligned}
M &= \int \sigma(r)(D+y)\,dy \\
&= \frac{1}{2} dP + \int \sigma(r)(r+d-R)\,dr \\
&= \frac{1}{2} dP - \frac{2E(m-1)hR^2}{3(1-\upsilon)m} \cdot \int \frac{r+d-R}{r^3} dr \\
&= \frac{1}{2} dP + \frac{2E(m-1)hR^2}{3(1-\upsilon)m} \cdot \left[\frac{1}{r} + \frac{d-R}{2r^2} \right] \Big|_{R-d}^{R-h} \\
&= \frac{1}{2} dP + \frac{2E(m-1)hR^2}{3(1-\upsilon)m} \left[\left(\frac{1}{R-h} - \frac{1}{R-d} \right) + \frac{d-R}{2} \left(\frac{1}{(R-h)^2} - \frac{1}{(R-d)^2} \right) \right]
\end{aligned} \tag{3-33}
$$

It can be seen from the above equations that the energy release rate induced by TGO growth remains constant as long as the TGO thickness stays fixed. However the TGO thickens during service at elevated temperatures, causing significant local stress increase.

The corresponding energy release rate from CTE in TGO and TBC is listed in Table II as follows.

Table II Energy release rate by TGO growth over TGO thickness

TGO thickness(m)	**G_{TGO}(Jm^2)**	**G_{TBC}**
5e-7	0.0024	1.0895
7e-7	0.0094	2.2145
e-6	0.0390	4.7761

The result above can be converted into the system's resistance to instant temperature drop or "temperature allowance". It can be taken into practice by relating with engine's temperature experience. Since the actual engine temperature scenarios can not be assessed definitively,

cooling trends from the situation of components are discussed in the following section.

3.3.2 Delamination maps

The delamination maps for deep delamination considering the effect of TGO under different conditions are plotted in Fig.3-3-5. Results at different TGO thickness are presented in Fig.3-3-6. The unshaded scales in Fig.3-3-5 are significantly diminished. It indicates that the system's endurance of initial surface temperature drop also declines– not being greater than substrate temperature change is essential for delamination prevention. In real conditions, TGO grows both in the lateral direction and normal to the interface, leading to a compression state during cooling process. The stress from displacement of TGO is normally perpendicular to the coating-substrate interface. As a result, the lateral residual stress of the TGO has a more predominant effect on mode I delamination than on mode II. This is reflected in Fig.3-3-5 and Fig.3-3-6 as the magnification of the reduction of unshaded area with increasing mode mix coefficient λ. In addition, with increased TGO thickness, the delamination-free area experiences a great reduction: for TGO thickness such as 0.7 μm and 1 μm, the safe area even disappears for certain mixed mode coefficients. The results prove the critical importance of TGO on coating delamination and thicker TGO indicates a higher tendency for coating delamination if considering the same cooling path. From Fig.3-3-5, it can be noted that the boundary of delamination starts upon $\Delta T_{sur/sub}$ equaling zero, it shows a difference from the result observed from thinner TGO. It indicates that when the TGO thickness increases, the system's tolerance to instant surface temperature drop decreases so rapid that any temperature change faster than the substrate will lead to coating delamination. In other words, backside cooling is required at the beginning of the engine operation and as entire temperature change increases, an even higher cooling rate is necessary to avoid delamination. In brief, thicker TGO leads to higher cooling requirement of engine system. In addition, the TGO thickness in the model is chosen as a fixed value, and to simulate the effect of TGO thickness evolution on failure behavior, more modeling work is required.

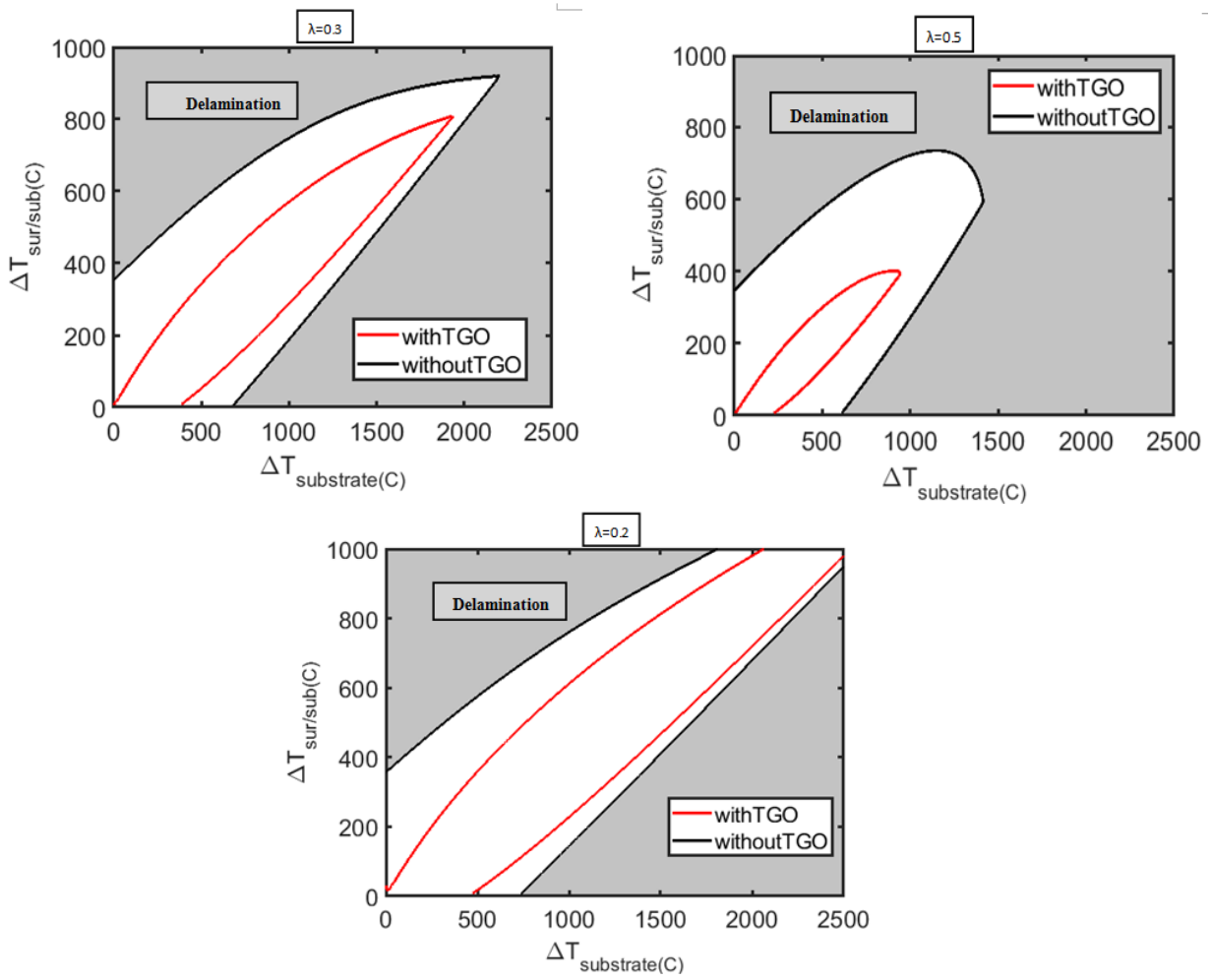

Fig.3-3-5 Delamination map for homogeneous coating with comparison of scenarios with and without TGO (h=5e-7): (a) λ=0.3, (b) λ=0.5, and (c) λ=0.2

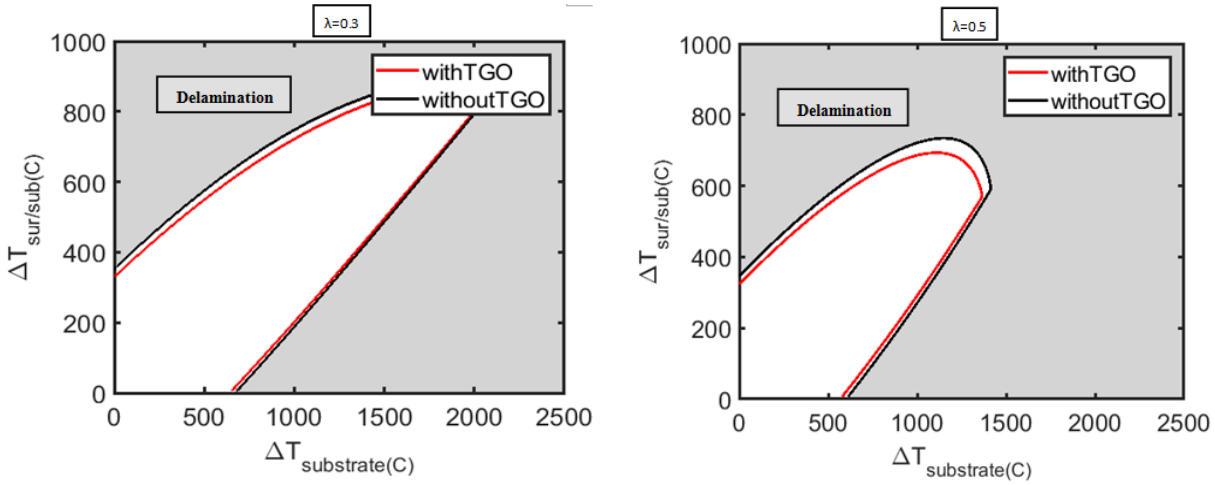

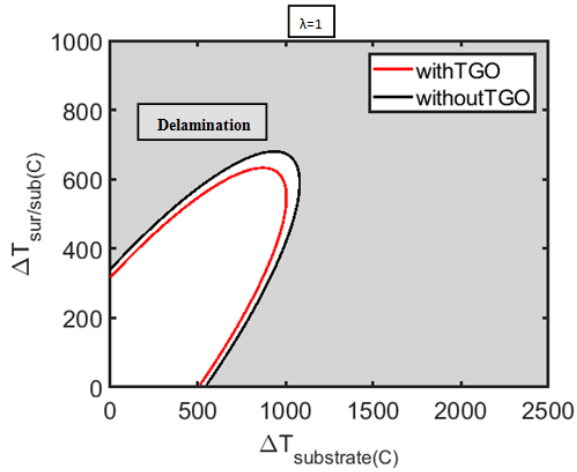

Fig.3-3-6 Delamination map for homogeneous coating with comparison of scenarios with and without TGO (h=1.8e-7).

(a) λ=0.3, (b) λ=0.5, and (c) λ=1

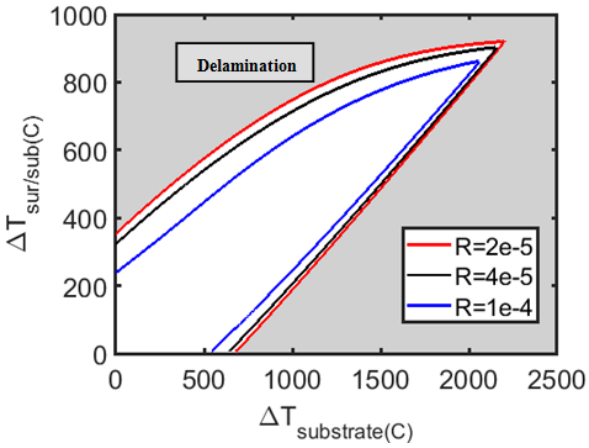

Fig.3-3-7 Delamination map with different imperfection radii (λ=0.3, h=1.8e-7).

The impact of the size of spherical imperfection is illustrated in Fig.3-3-7. It shows an obvious trend that larger imperfection indicates smaller delamination free zone. From previous research, a certain degree of interface roughness is found to be beneficial in preventing crack propagation. The peak of the interface will act as a barrier to the crack propagation, illustrating an anchor effect.

3.4 Conclusions

The research in this chapter is based on the earlier work from Evans and Hutchinson [16][21].

A spherical model is combined with the existing bi-layer system to analyze the effect of thermal gradient and thermally grown oxide on delamination behavior for the undulated coating interface. Detailed discussion is presented for delamination at the interface between top coat and substrate and shallow crack near the coating surface. Delamination maps were established for coatings where the TGO thicknness and its interface morphology are taken into consideration.

CHAPTER 4. CYCLIC OXIDATION MODELLING

4.1 Methodology

In this chapter, two models of life time prediction of coating under cyclic oxidation are combined. The two models are: the COSP model by NASA [22] and a mechanic based model by K. CHAN [23]. The COSP model is an iterative process to describe the spall modes, while the mechanics based model focuses on the mechanics of spallation caused by pre-existing shear cracks. Predictions are made with the modified model and validations are made by comparison with experiment data. The goal of this part of this chapter is to improve the life time prediction efficiency.

Cyclic oxidation of protective coatings occurs during aircraft landing and taking off. The difference between thermal expansion coefficients of the layers will lead to a large residual stress. When coatings experience repeated heating and cooling, the crack size will accumulate and cause coating spallation which will cause the total weight of coating to change during cycling. It is of significant importance to analyze the weight change as a way to determine the coating's life time.

4.1.1 Weight change curve

Many experiments have been carried out to investigate the total weight variation of an alloy sample during cyclic oxidation to evaluate the coating life time, as shown in Fig.4-1-1. However, it can be both expensive and time consuming. For example, in Fig.4-1-1, for experiments under 1200℃, it requires 3000h, more than four months to run the complete test. For tests under lower cycling temperature, the time scale required is even much longer. Therefore, life time prediction models are employed. However, as required by the COSP model, the weight change curve needs to reach a negative value and approach a linear relationship with cycle time to provide sufficient input parameter for predictions.

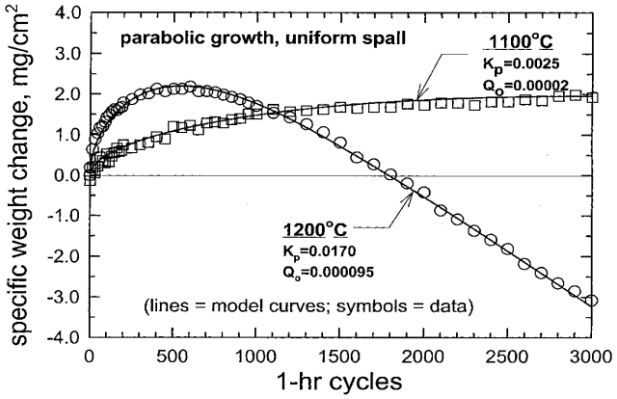

Fig.4-1-1 Fitted COSP model curves with 1100℃ and 1200℃ cyclic oxidation data for NiAl+0.1Zr using 1-hr cycles [22] .

In the following section, an introduction of the weight change curve and the method of calculating the iterative process of oxidation and spallation are given. Here, the *x* axis represents cycle number and *y* is the specific weight change. The total weight change curve always shows an upward trend in the beginning due to the high rate of oxidation and low rate of spallation. The curve falls when the balance reverses. The higher the maximum experiment temperature is, the sharper the curve becomes. It can be inferred that under relatively low testing temperature, the time and cost required to run through a completed experiment can be tremendous. The life time prediction model can therefore be improved by predicting the complete curve of material behavior with the shortest possible experiment time and extending the results to different conditions.

The two main causes of the weight change are the oxide scale formation during heating cycle and spallation during cooling cycle. The delamination mechanics of protective coating under cyclic oxidation have been widely analyzed and different models have been developed to quantify growth and spallation behavior. One of the most accepted models employed in the investigation is the COSP (Cyclic Oxidation Spall Program).

Oxidation growth kinetics is described by the following equation, in terms of the parabolic growth law:

$$W_{ox} = a \cdot \sqrt{k_p t} \tag{4-1}$$

where W_{ox} is the total weight of oxide formed, a is the ratio of the molecular weight of the oxide

to the molecular weight of oxygen, and k_p is the parabolic rate constant.The weight of oxide spall in each cycle W_s as a monotonic function of oxide thickness (reflected by oxide remained before cooling in one cycle W_r) can be expressed as:

$$W_s = F \cdot W_r' \tag{4-2}$$

where F is the fraction of oxide spalled and W_r' is the remaining weight before cooling. It has been observed that F is linearly proportional to W_r', given the coefficient Q_0:

$$F = Q_0 \cdot W_r' \tag{4-3}$$

To determine Q_0, the thermogravimetric apparatus (TGA) was used to obtain the amount of oxide formed. At the same time, the fraction of oxide spalled was determined by comparing the weight change before and after the cycle. With the plot of the spallation fraction F against the specific weight of oxide remained before cooling, Q_0 can be obtained as the slope of the straight line in Fig.4-1-2.

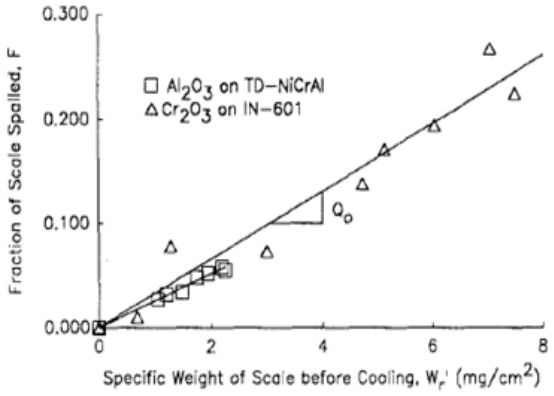

Fig.4-1-2 Spallation fraction F as dependence of oxide spalled with the specific weight of oxide remains before cooling for Cr_2O_3 and Al_2O_3 [13].

To predict the alloy oxidation behavior at specific experimental conditions, the equations are given in Table III, based on input parameters a, τ, k_p, Q_0.

Table III Equations for Cyclic Oxidation Derived from COSP Parabolic Oxide Growth and Uniform Layer Spalling

A.General regression equations

$$\log(\boldsymbol{C}_0) = \boldsymbol{B}_{11} + \boldsymbol{B}_{12}\log(\boldsymbol{a}) + \boldsymbol{B}_{13}\log(\boldsymbol{k_p}) + \boldsymbol{B}_{14}\log(\boldsymbol{Q}_0) + \boldsymbol{B}_{15}\log(\boldsymbol{\tau})$$

$$\log\left((\Delta \boldsymbol{W} / \boldsymbol{A})_{\max}\right) = \boldsymbol{B}_{21} + \boldsymbol{B}_{22}\log(\boldsymbol{a}) + \boldsymbol{B}_{23}\log(\boldsymbol{k_p}) + \boldsymbol{B}_{24}\log(\boldsymbol{Q}_0) + \boldsymbol{B}_{25}\log(\boldsymbol{\tau})$$

$$\log(\dot{\boldsymbol{W}}_{\boldsymbol{m}}) = \boldsymbol{B}_{31} + \boldsymbol{B}_{32}\log(\boldsymbol{a}) + \boldsymbol{B}_{33}\log(\boldsymbol{k_p}) + \boldsymbol{B}_{34}\log(\boldsymbol{Q}_0) + \boldsymbol{B}_{35}\log(\boldsymbol{\tau})$$

B. Regression equations with derived coefficients

$$\log(\boldsymbol{C}_0) = 0.61 - 1.9\log(\boldsymbol{a}) - 0.33\log(\boldsymbol{k_p}) - 0.67\log(\boldsymbol{Q}_0) - 0.34\log(\boldsymbol{\tau})$$

$$\log\left((\Delta \boldsymbol{W} / \boldsymbol{A})_{\max}\right) = -0.17 - 0.76\log(\boldsymbol{a}) + 0.33\log(\boldsymbol{k_p}) - 0.34\log(\boldsymbol{Q}_0) + 0.33\log(\boldsymbol{\tau})$$

$$\log(\dot{\boldsymbol{W}}_{\boldsymbol{m}}) = -0.71 + 2.0\log(\boldsymbol{a}) + 0.67\log(\boldsymbol{k_p}) + 0.33\log(\boldsymbol{Q}_0) + 0.67\log(\boldsymbol{\tau})$$

Coefficients of variables are obtained from multiple linear regressions of results from systematically varied input parameters, and it is proved to be applicable to different alloys and conditions.

4.1.2 Effective time from different model

To calculate the growth of the oxide, taking spallation into consideration, the effective time t_e was proposed and determined as the time required to obtain the equal specific weight of the oxide as in an isothermal test. In NASA's work [22], for any circle j,t_e is given as:

$$t_{ej} = (t_{e(j-1)} + \tau)[1 - a \cdot k_p^{1/2} \cdot Q_0 (t_{e(j-1)} + \tau)^{1/2}]^2 \quad (4\text{-}4)$$

Another model by Chan is taken into consideration [23]. The schematic diagram of the model is shown in Fig.4-1-3, where the shear crack induced by thermal stress during cooling down develops wing tip cracks. These wing tip cracks propagate and link with the othershear crack, causing the separation of the oxide.

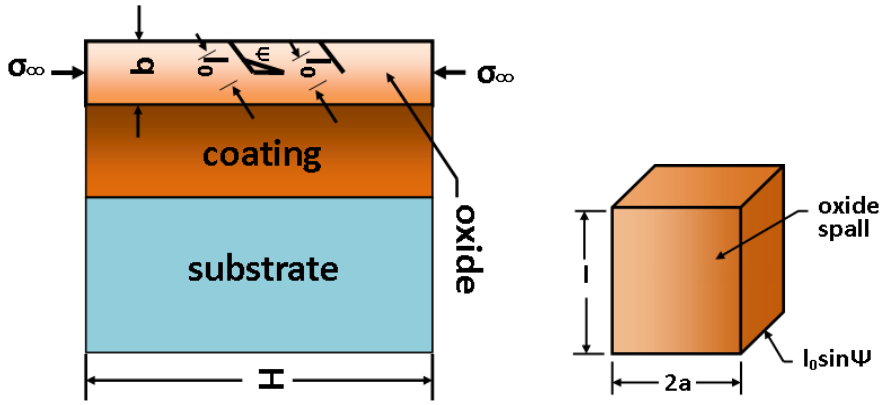

Fig.4-1-3 Schematic of mechanic based model by Chan [23].

In Chan's work [23], the effective time after *j* cycle is given by:

$$t_{ej} = [t_{e(j-1)} + \tau][1 - q\Delta T^2 W_{ox}] \tag{4-5}$$

where *q* is the spallation constant determined by microscopic parameters such as crack density, average length of shear crack, angle between shear crack and compressive stress axis , Young's modulus and fracture toughness.

4.1.3 Spallation parameters

By combining the two equations of effective time (4-4) and (4-5), another expression of the relationship between *q* and t_e is obtained:

$$q = \left[-a \cdot \sqrt{k_p} \cdot Q_0^2 \left(\frac{t_{e(j-1)} + \tau}{\sqrt{t}} \right) + 2 \cdot Q_0 \left(\frac{t_{e(n-1)} + \tau}{t} \right)^{1/2} \right] / \Delta T^2 \tag{4-6}$$

At the first cycle of the oxidation, t_{e1} can be obtained from equation (4-4) and then substituted into equation (4-6) for the solution of *q* in the corresponding cycle when *j* is set as two. Different from that in Chan's work, *q* is time dependent in the current model. The t_{e1} will then be used for the next cycle. The rest of the calculation of the cycles follows the same procedure. After *q* for each cycle is obtained, it becomes possible to calculate *m* for certain alloy, which represents the crack density variation with respect to volume. The approach of calculating *m* from cyclic oxidation data is given as:

$$W_s = q\Delta T^2[\frac{W_{ox}}{W_0}]^{1+m} \tag{4-7}$$

Therefore, *m* can be written as:

$$m = \frac{\log W_s}{\log\left[q\Delta T^2\left(\frac{W_{ox}}{W_0}\right)\right]} - 1 \tag{4-8}$$

The above equations indicate that *m* also changes with the cycle.

By imposing experimentally measured data, *q* can be obtained by:

$$q = \frac{\tau}{2Zt_m\Delta T^2}\left[1+\frac{\tau}{2t_m}\right]^{-(1+m)} \cdot \left[\frac{W_0}{Z\sqrt{k_p t_m}}\right]^m \tag{4-9}$$

Thus, one has:

$$m = \frac{\log\left[\frac{qZ\Delta T^2\left(2t_m+\tau\right)}{\tau}\right]}{\log\left[\frac{2t_m W_0}{Z\sqrt{k_p t_m}\left(2t_m+\tau\right)}\right]} \tag{4-10}$$

Equation (4-10) makes it achievable to obtain the value of *m* using only one experimental value t_m,i.e., the time when weight change reaches the maximum. This simplified equation allows prediction based on "incomplete curve" which means the curve begins to show a downtrend. In addition, Q_0 can be obtained through the second equation in Table II with the maximum of weight change and given the value of $k_p.t_m$ can be obtained by fitting experimental data and calculating the maximum value of the fitting curve.

4.2 Modeling results and discussions

Fig.4-2-1shows the measured data and curves of weight changes by Chan on a stainless steel Fe-Ni-Cr-Al. The test was performed between a peak temperature of 1200℃ and a minimum temperature of 25℃ for cycle duration of 20h. k_p equals 0.011mg^2/cm^4/h. The calculated curve appears to be in good agreement with the experiment data. However, according to the

original paper, even though the equations of q and m based on available data were derived analytically, the result for q was obtained through adjusting other input parameters in an experience manner, and with this well-adjusting q, a curve in good agreement with the data was obtained.

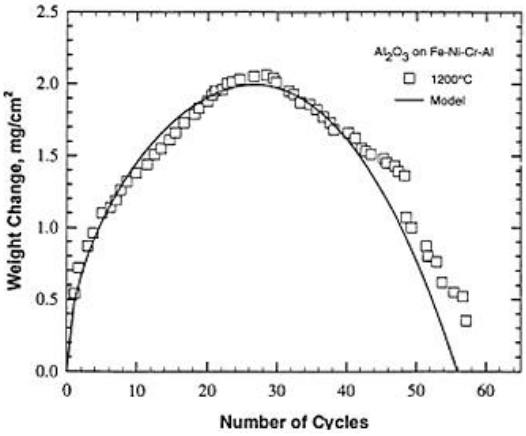

Fig.4-2-1 Model fitted curve and experimental data of Al_2O_3 on Fe-Ni-Cr-Al under cyclic oxidation of 1200℃ [23].

To apply the new model to this same data, only t_m is needed. To find its value, a polynomial is fit to the data, which gives:

$W_c = 0.40463 + 0.12157n - 0.00246n^2 - 5.19e-6n^3$. Experiment data is fitted to obtain the time when the weight change reaches maximum. The corresponding time when W_c reaches the maximum is calculated to be t_m=540h. Since experiment data obtained in this research is limited, and different fitting functions can be applied, t_m will change slightly. However, the value of m is found to be sensitive to t_m. Therefore it is necessary to compare the original curve plotted using the unchanged parameter, as shown in Fig.4-2-6. (Otherwise it will be pure fitting.) Decreasing the t_m value leads to increase in m and reduction in W_c. Fig.4-2-2 shows measured and calculated curves using t_m=560h and good agreement are obtained.

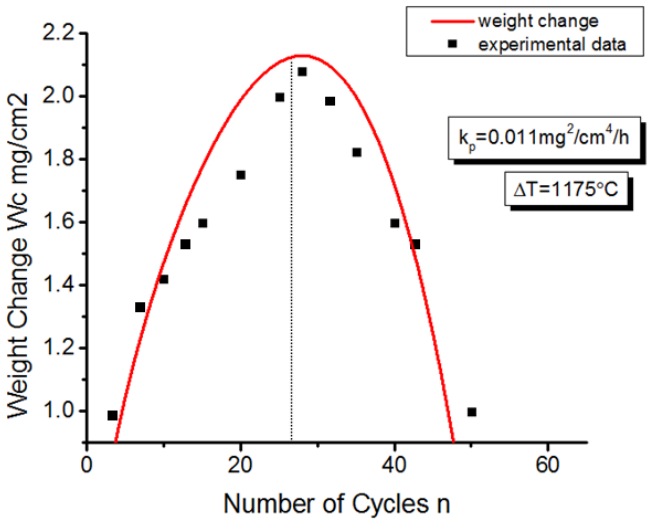

Fig.4-2-2 Calculated weight change and experimental data of Al_2O_3 on Fe-Ni-Cr-Al under cyclic oxidation of 1200℃, t_m=560h.

Under the same conditions, the trends of q and m are shown in Fig.4-2-3. The value of q declines over time, while m increases.

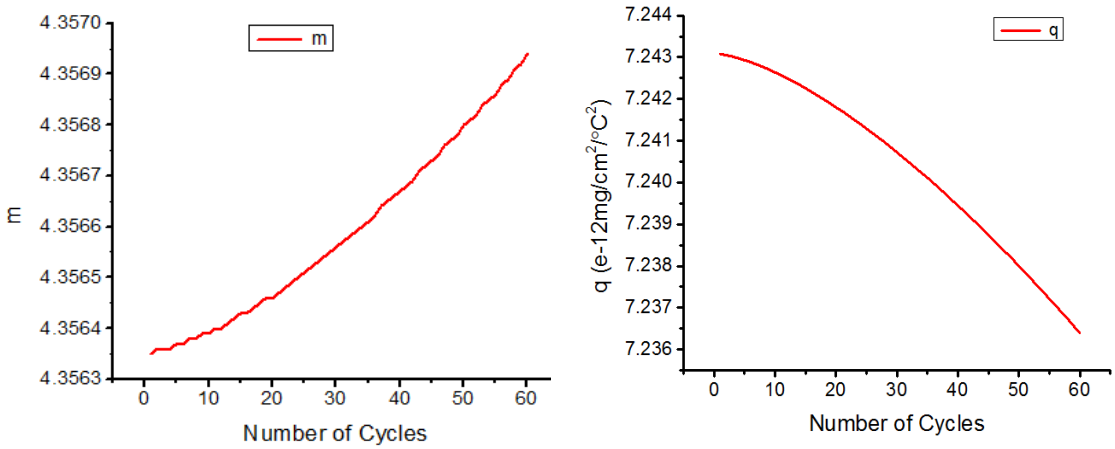

Fig.4-2-3 Variation of spallation parameter m and q over cycle number.

The weight of remaining oxide on the alloy is expressed in NASA ‘s work as:

$$W_r = a \cdot \sqrt{k_p \cdot t_{en}} \tag{4-11}$$

while in Chan’s work: $W_r = W_{ox} - W_s$. The expression of W_r may cause confusion in the definitions of W_{ox} and W_s. W_{ox} and W_r are defined as the amounts of oxide that forms and remains respectively in total in one test but W_s is the measured amount of spallation in one

cycle. Therefore, Chan's expression is considered to be inaccurate and will result in larger value of remaining weight. To be more accurate in prediction of weight change, the equation is modified as:

$$W_r = a \cdot \sqrt{k_p \left(t_{en} - \tau\right)} + a \cdot \sqrt{k_p t} - a \cdot \sqrt{k_p \left(t - \tau\right)} - W_s \tag{4-12}$$

Considering the value of W_s can be relatively small compared to the other two, the calculated results may not show obvious contrast.Comparison of the three approaches is presented in Fig.4-2-4:

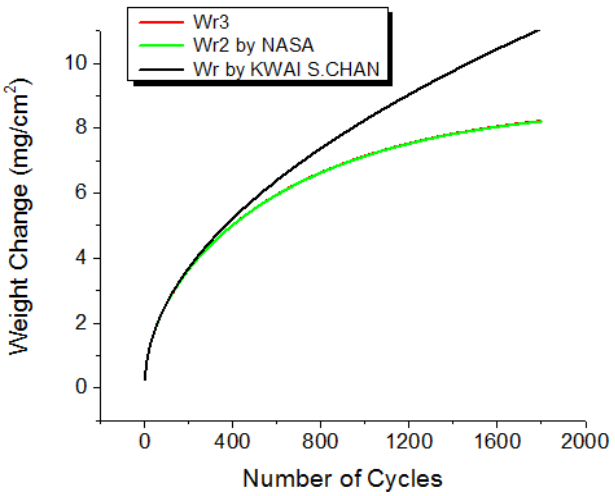

Fig.4-2-4 Weight remaining after each heating cycle from different models.

In this experiment, the three curves follow a similar trend and the value is fairly close considering the big difference of magnitude between W_s and W_{ox}.

For further verification of the model, the comparison of calculated and measured data of weight change associated with cycling of Ni-48.3Al-0.1Zr subjected to 1-h thermal cycles between a maximum of 1200℃ and a minimum temperature of 60℃ presented as follows. The experiment data and prediction result by Chan are presented in Fig.4-2-5 (k_p is given as 0.0151mg^2/cm^4/h).

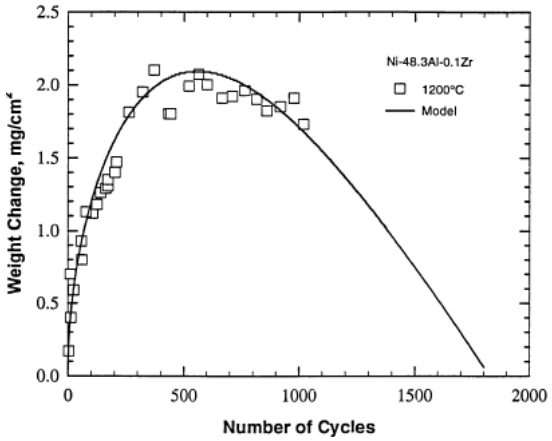

Fig.4-2-5 Experimental data and fitted curve of Ni-48.3Al-0.1Zr under cyclic oxidation of 1200℃ [23].

The expression of the curve fitted by polynomial approach is:

$$W_c = 0.222 + 0.00948n + (-1.745 \cdot 10^{-5}) \cdot n^2 + 1.362 \cdot 10^{-8} \cdot n^3 - 4.140 \cdot 10^{-12} \cdot n^4$$

The theoretical maximum of W_c should be obtained when t_m=500h. Good agreement between calculated result and experimental data can be acquired with t_m=450h, given the proportion of adjustment being 10% (shown in Fig.4-2-6(a)). The corresponding curve plotted with $t_m = 500\text{h}$ is also shown in Fig.4-2-6(b) as a contrast to prove that the model is of certain accuracy without any adjustment of the parameters. The remaining weight and spallation loss curves are plotted in Fig.4-2-7.

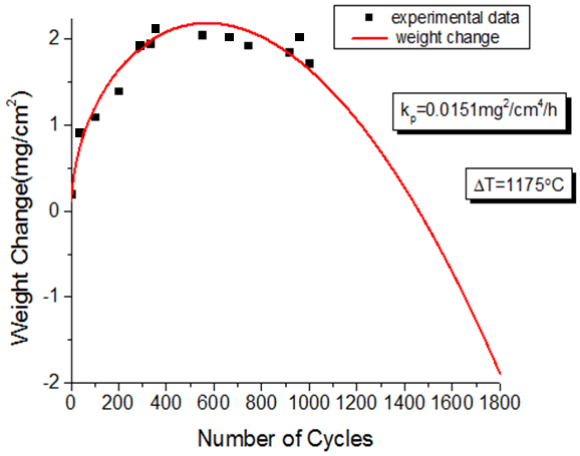

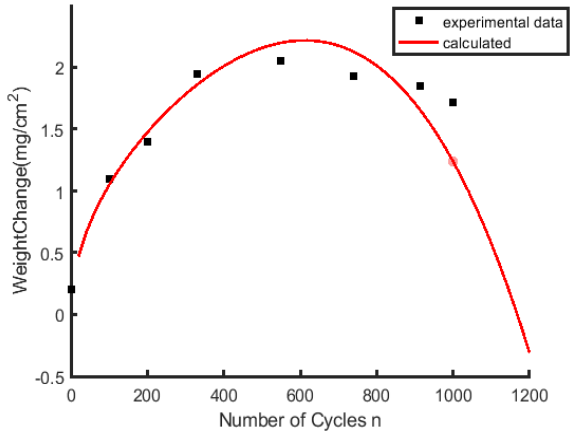

Fig.4-2-6 (a)Total weight change of Ni-48.3Al-0.1Zr from calculation with t_m=450h. (b)calculation result with t_m =500h.

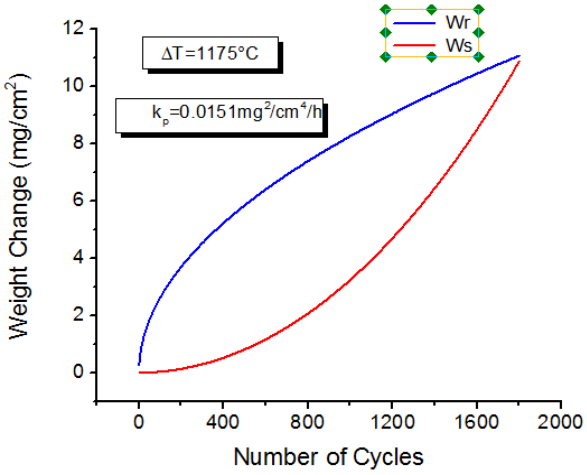

Fig.4-2-7 Remaining weight and spallation of Ni-48.3Al-0.1Zr of different number of cycles.

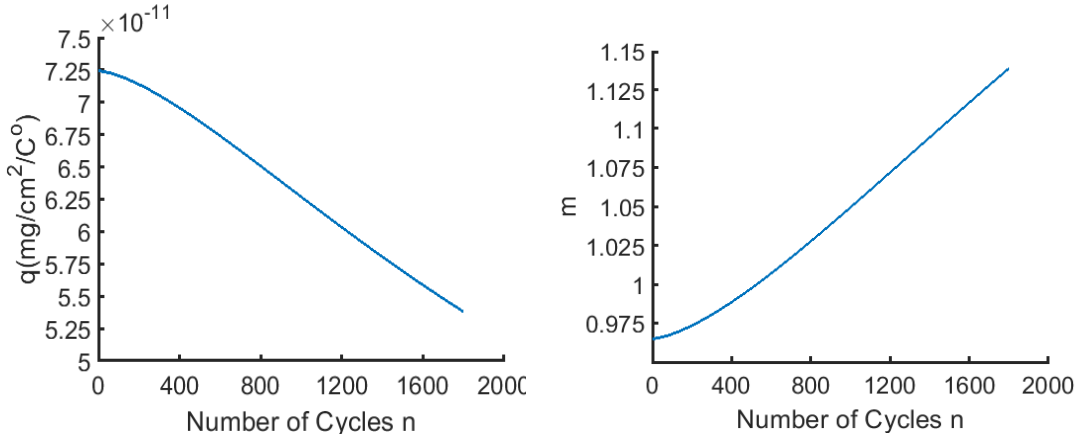

Fig.4-2-8 Dependence of parameter *q* and *m* on different number of cycles (Ni-48.3Al-0.1Zr).

Fig.4-2-8 shows the relevant curve of *q* and *m* from the model. Both of them are reasonable compared to that in Chan's work where *m*=1 and *q*=7.5e-11.

The proposed model is used to predict the oxidation behavior of different material with 'insufficient' experimental data—incomplete curve. While required experiment time is significantly reduced, the complete behavior of single experiment as well as behavior under different conditions can be predicted. In Fig.4-2-9, the weight change data of Fe-Ni-Cr-Al under 20-h thermal cycle with the maximum of 1200℃ is applied to the model, k_p equals 0.011mg^2/cm^4/h.

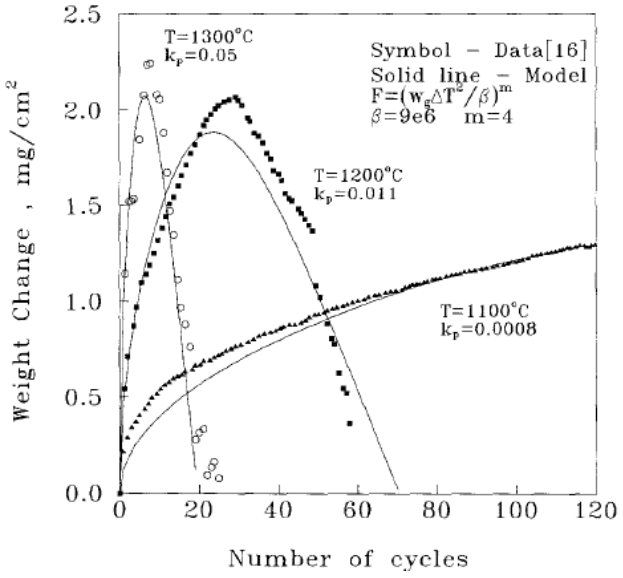

Fig.4-2-9 Experimental weight-change data for Fe-Ni-Cr-Al at various temperatures [24].

The t_m obtained from fitting is 550h and a good agreement between the calculated and measured data is reached when t_m is adjusted to be 560h.

The calculated curve using data from Fig.4-2-9 is compared against the experimental data in Fig.4-2-10. W_r *and* W_s after each cycle calculated by three different methods are presented in Fig.4-2-11. The dependence of m and q on the number of cycles is given in Fig.4-2-12.The values of m and q varied around 4.35 and 7.2e-12 showing upward and downward trends respectively.

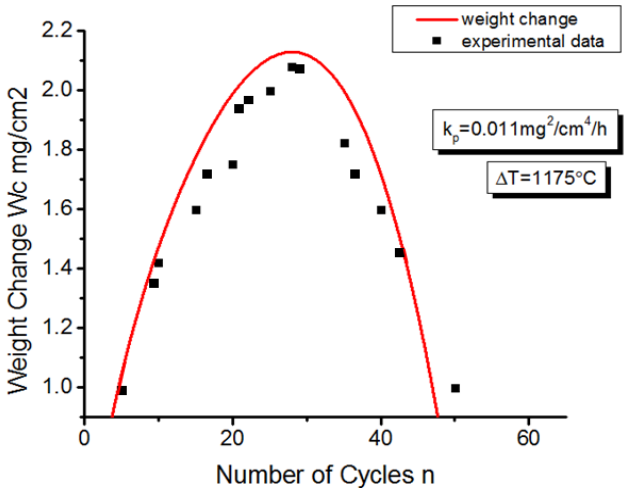

Fig.4-2-10 Comparison of calculated and measured weight change for Fe-Ni-Cr-Al at 1200℃.

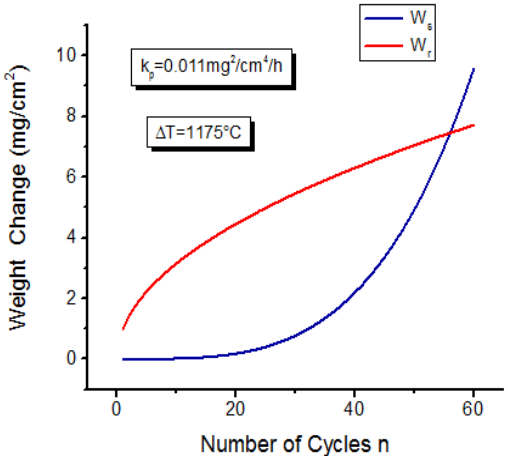

Fig.4-2-11Calculated weight loss and remaining weight for Fe-Ni-Cr-Al at 1200℃.

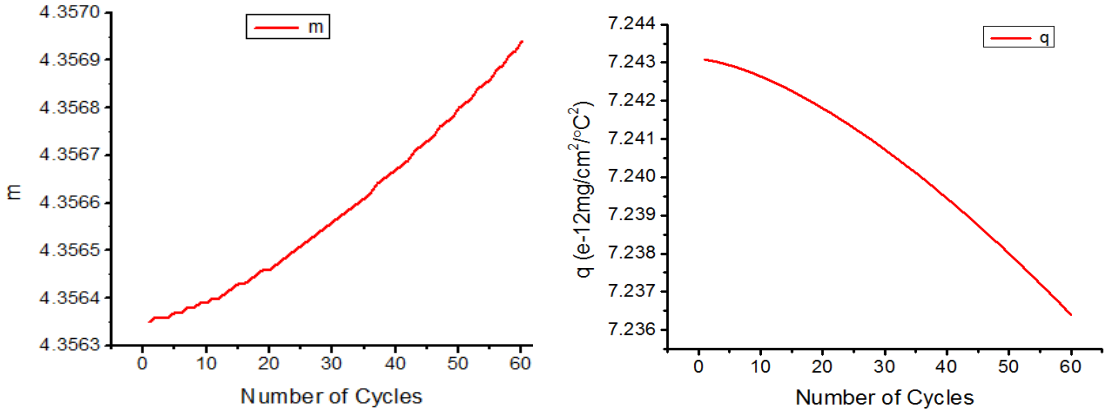

Fig.4-2-12 Dependence of spallation parameter *m* and *q* on number of cycles (Fe-Ni-Cr-Al).

Using data provided by NASA in Fig.4-1-1, which shows the maximum of specific weight

change, values of *q*, *m* and *Wr* are obtained. Here, t_m is calculated to be 570h and without any modification, behavior of the material is successfully predcted as shown in Fig.4-2-13. Similar trends of *q* and *m* can be observed.

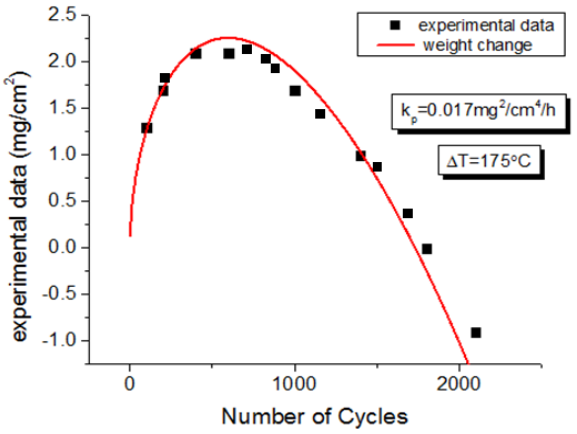

Fig.4-2-13 Calculated and experimental data of NiAl-0.1Cr under cycles of 1200℃.

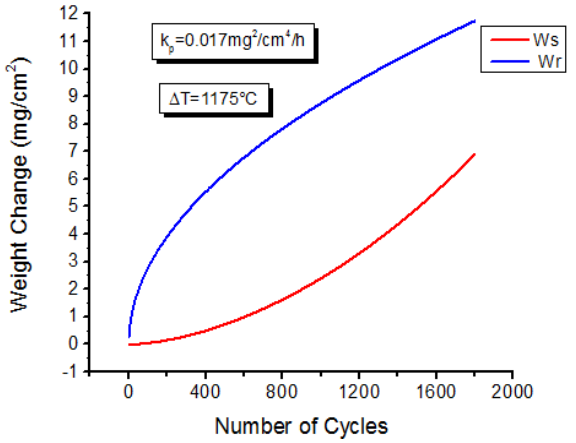

Fig.4-2-14 Calculated weight loss and remaining weight for NiAl-0.1Cr at 1200℃.

From previous work, the value of *m* is discovered to be mainly dependent on the location of fracture during spallation. *m*=0 is for complete interface spallation and *m*=1 is for complete bulk spallation. The upward trend of *m* shown in Fig.4-2-8 and Fig.4-2-12 indicates that the fracture mode of material slightly changes as the number of cycles increases. Different from results in Chan's work, bulk spallation is shown to present in certain material mentioned.

4.3 Conclusion

Based on the cyclic oxidation models developed by Chan and NASA, two key model parameters called spallation parameters q and m are modified to be time dependent. A new approach of calculating q and m from experimental data is also proposed. q is found to decrease as the number of cycles increases while m shows an opposite trend over time. The value of parameter m depends on the location of fracture during spallation and the trend reveals that cracks tend to show a transformation from interface spallation to a mix of interface spallation with bulk spallation.

The modified model is able to predict further cyclic behavior of coatings based on an "incomplete curve" which only requires the curve to show a downward trend after peak value. Shorter experiment time is proven to be sufficient to predict coating life time and spallation behavior under different conditions. The model can be further improved by considering the time that the experiment data should include to reduce the error caused by the sensitivity of t_m. Also, the development of the coating's elastic properties can be taken into consideration to improve the model accuracy.

CHAPTER 5. CONCLUSION AND FUTURE RESEARCH IMPLICATIONS

In the above two chapters, protecting coatings' behaviors under thermal gradient conditions and cyclic oxidation are investigated respectively.

The results of coating delamination mechanics over thermal gradients are presented for homogenous coatings with deep and shallow delamination locations. A spherical model is combined with a frequently used multilayer model to generate results closer to actual conditions. Two more key factors are added to the model: TGO and interface roughness. The critical TGO effect is considered by inducing stresses from CTE mismatch and TGO growth. Detailed analysis is presented for several sets of TGO thickness, imperfection size and mode mix parameters. The influence of the factors on temperature allowance and cooling requirements are analyzed. Delamination maps are established to analyze the influence of different cooling trajectories on delamination incidence. It reveals that the delamination incidence is sensitive to the cooling trajectory, even with the same initial temperature distribution. The safest trajectory with corresponding instantaneous temperature drop that will prevent coating delamination and crack propagation is therefore suggested. For future research, a well specified temperature experience by the coating in actual engine is needed through experimental assessment to further validate the model.

In cyclic oxidation modeling, an approach to obtain the spallation parameter from experimental data based on equivalent time is presented. The dependence of parameter q and m, for complete interface spallation, on time is obtained and analyzed. A crucial factor, time to reach the maximum scale weight change, is applied to predict coating behavior within the shortest possible experment time. The accuracy of the proposed model is demonstrated by comparing experimental data and model calculation results.

For future assessment, the change of the material characteristic such as Young's modulus,

fracture toughness and TGO thickness under cyclic condition can be taken into consideration for results with more fidelity. In addition, the applicability and accuracy of the proposed model to predict the behavior of material behavior under different cyclic oxidation conditions will be verified.

Reference

[1] N. P. Padture, M. Gell, E. H. Jordan, Thermal barrier coatings for gar-turbine engine application, Science, Vol.**296**, 2002, pp.280-284.

[2] M. P. Bacos, J. M. Dorvaux, O. Lavigne, R. Mevrel, M. Poulain, Performance and Degradation Mechanics of Thermal Barrier Coatings for Turbine Blades: A Review of Onera Activities, High Temperature Material, (2001).

[3] P. K. Wright, A. G. Evans, Mechanisms governing the performance of thermal barrier coatings, Current Opinion in Solid State and Material Science, Vol.**4**(1999), pp.255-265.

[4] Z. Tang, H. Kim, I. Yaroslavski, G.Masindo, Z. Celler, D.Ellsworth, Novel Thermal Barrier Coatings Produced by Axial Suspension Plasma Spray, International Thermal Spray Conference and Exposition, 2011.

[5] K. V. Every, Matthew J. M. Krane, R. W. Trice, H. Wang, Column formation in suspension plasma-sprayed coatings and resultant thermal properties, Journal of Thermal Spray Technology, Vol.**20**(4), 2011, pp.817-828.

[6] M. Karger, R. Vaben, D. Stover, Atmospheric plasma sprayed thermal barrier coatings with high segmetation crack densities:Spraying process, micro structure and thermal cycling behavior,Surface and Coatings Technology, Vol.**206**(2011), pp.16-23.

[7] B. D. Choules, Klod Kokini, T. A.Taylor, Thermal fracture of ceramic thermal barrier coatings under heat flux with time-dependent behavior, Material Science and Engineering, Vol.A**299**(2001), pp.296-304.

[8] D. R. Clarke, C. G. Levi, Material design for the next generation thermal barrier coatings, Annual Review of Materials Research,Vol.**33**(2003), pp.383-417.

[9] A. Rabiei, A. G. Evans, Failure mechanisms associated with the thermally grown oxide in plasma-sprayed thermal barrier coatings, Acta Materialia, Vol.**48**(2000), pp.3963-3976.

[10] M. J. Stiger, G. H. Meier, F. S. Pettit, Q. Ma, J. L. Beuth, M. J. Lance, Accelerated cyclic oxidation testing protocols for thermal barrier coatings and alumia-forming alloys and coatings, Materials and Corrosion, Vol.**57**(2006), pp.73-85.

[11] A. M. Karlsson, J. W. Hutchison, A. G. Evans, A fundamental model of cyclic instabilities

in thermal barrier systems, Journal of the Mechanics and Physics of Solids, Vol.**50**(8),2002, pp.1565-1589.

[12] D. Poquillon, D. Monceau, Application of a simple statistical spalling model for the analysis of high-temperature, cyclic oxidation kinetics data, Oxidation of Metals, Vol.**59**(2003), pp.409-431.

[13] C. E. Lowell, C. A. Barrett, R. W. Palmer, J. V. Auping, H. B. Probst, COSP: A computer model of cyclic oxidation, Oxidation of Metals, Vol.**36**(1991), pp.81-112.

[14] D. Poquillon, D. Oquab, D, Monceau, Cyclic oxidation kinetics of modeling of NiAl single crystal, Materials Science Forum, 2004, pp.737-745.

[15] J. L. Smialek, Universal characteristics of an interfacial spalling cyclic oxidation model, ActaMaterialia, Vol.**52**(2004), pp.2111-2121.

[16] A. G. Evans, J. W. Hutchinson, The mechanics of coating delamination in thermal gradients, Surface and Coating Technology, Vol.**201**(2007), pp. 7905-7916.

[17] M. Martena, D. Botto, P. Fino, S. Sabbadini, M. M. Gola, C. Badini, Modelling of TBC system failure: Stress distribution as a function of TGO thickness and thermal expansion mismatch, Engineering Failure Analysis, Vol.**13**(2006), pp.409-426.

[18] A. G. Evans, D. R. Mumm. J. W. Hutchinson, G. H . Meier, F. S. Pettit, Mechanisms controlling the durability of thermal barrier coatings, Progress in Materials Science, Vol.**46**(2001), pp.505-553.

[19] A. C. Fox, T. W. Clyne, Oxygen transport by gas permeation through the zirconia layer in plasma sprayed thermal barrier coatings, Surfaces and Coatings Technology, Vol.**184**(2004), pp.311-321.

[20] M. Z. Dong, R. A. Miller, Thermal conductivity and elastic modulus evolution of thermal barrier coatings under high heat flux conditions, Journal of Thermal Spray Technology, Vol.**9**(2), 2000, pp.175-180.

[21] A. G. Evans, M. Y. He, J. W. Hutchinson, Mechanics-based scaling laws for the durability of thermal barrier coatings, Progress in Materials Science, Vol.**46**(2001), pp.249-271.

[22] J. M. Smialek, J. V. Auping, COSP for Windows-Strategies for Rapid Analysis of Cyclic-Oxidation Behavior, Oxidation of Metals, Vol.**57**(2002), pp.559-581.

[23] K. S. Chan, A mechanics-based approach to cyclic oxidation, Metallurgical and Materials Transactions, Vol.**28**A(1997), pp.411-422.

[24] Chang-Oh Moon, Soon-Bok Lee, Analysis on Failures of Protection –Oxide Layers and Cyclic Oxidation, Oxidation of Metals, Vol.**39**(1993), pp.1-13.

[25] G. Qian, T. Nakamura, C. C. Berndt, Effects of thermal gradient and reidual stresses on thermal barrier coating fracture, Mechanics of Materials, Vol.**27**(1998), pp.91-110.

[26] A. G. Evans, J. W. Hutchinson, On the mechanics of delamination and spalling in compressed films, International Journal of Solids and Structures, Vol.**20**(5), 1984, pp.455-466.

[27] Z. Xue, A. G. Evans, J. W. Hutchinson, Delamination Susceptibility of Coatings Under High Thermal Flux, Journal of Applied Mechanics, Vol.**76**, 2009, pp.1-7.

[28] K. Kokini, A. Banerjee, T. A. Taylor, Thermal fracture of interfaces in precracked thermal barrier coatings, Material Science and Engineering,Vol. A**323**(2002), pp.70-82.

[29] S. Rangaraj, K. Kokini, Estimating the fracture resistance of functionally graded thermal barrier coatings from thermal shock tests, Surface and Coatings Technology, Vol.**173**(2003), pp.201-212.

[30] Y. Tan, J. P. Lontin, S. Sampath, M. J. Dong, Temperature gradient effects in thermal barrier coatings: an investigation through modeling, high heat flux test and embedded sensor, Journal of American Ceramic Society, Vol.**93**(10), 2010, pp.3418-3426.

[31] C. Mercer, S. Fauhaber, A. G. Evans, R. Darolia, A delamination mechanism for themal barrier coatings subject to calcium-magnesium-alumino-silicate (CMAS) infiltration, C. Mercer et al. Acta Materialia, Vol.**53**(2005), pp.1029-1039.

[32] M. J. Stiger, N. M. Yanar, M. G. Topping, F. S. Pettit, G. H. Meier, Z.Met. kd, Vol.**90**(1999)1069.

[33] J. W. Hutchison, Z. Suo, Mixed mode cracking in layered materials, Advances in Applied Mechanics, Vol.**29**(1992), 63.

[34] O. Trunova, Effect of thermal and mechanical loadings on the degradation and failure modes of APS TBCs, Dissertation, RWTH Aachen, 2006.

[35] Z. Suo, J. W. Hutchinson, Steady-state cracking in brittle substrate beneath adherent film, International Journal of Solids and Structures, Vol.**25**(1998), pp.1337-1353.

[36] J. A. Haynes, M. K. Ferber, W. D. Porter, E. D. Rigney, Characterization of alumina scales formed during isothermal and cyclic oxidation of plasma-sprayed TBC systems at 1150℃, Oxidation of Metals, Vol.**52**(1999), pp.31-76.

[37] N. M. Yanar, F. S. Pettit, G. H. Meier, Failure characteristic during cyclic oxidation of Yttria stabilized Zirconia TBC deposited via EBPVD on Platinum aluminide and on Ni-Co-Cr-Al-Y bond coats with processing modifications for improved performance, Metalluergical and Materials Transactions, Vol.**37**A(2006), pp.1563-1580.

[38] H. Echsler, V. Shemet, Cracking in and around thermally grown oxide in thermal barrier coatings: A comparison between isothermal and cyclic oxidation, Journal of Material Science, Vol.**41**(2006), pp. 1047-1058.

[39] M. Z. Dong, R. A. Miller, Determination of Creep Behavior of Thermal Barrier Coatings Under Laser Imposed Temperature and Stress Gradients, NASA Technical Memorandum, 1997.

[40] N. A. Fleck, A. C. F. Cocks, S. Lampenscherf, Thermal shock resistance of air plasma sprayed thermal barrier coatings. Journal of the European Ceramic Society, Vol.**34**(2014),pp. 2687-2694.

[41] S. Rangaraj, K. Kokini, Estimating the fracture resistance of functionally grade thermal barrier coatings from thermal shock tests, Surface and Coatings Technology, Vol.**173**(2003), pp.201-212.

[42] K. Kokini, A. Banerjee, T. A. Taylor, Thermal fracture of interfaces in precracked thermal barrier coatings, Materials Science and Engineering, Vol.**323**A (2002): pp. 70-82.

[43] B. D. Choules A, K. Kokini, T. A. Taylor, Thermal fracture of thermal barrier coatings in a high heat flux environment. Surface and coatings Technology, Vol.**106** (1998), pp. 23-29.

[44] T. J. Lu, N. A. Fleck, The Thermal Shock Resistance of Solids, Acta Materia, Vol.46(1998), pp.4755-4768.

[45] S. R. Choi, J. W. Hutchinson, A. G. Evans, Delamination of multilayer thermal barrier coatings. Mechanics of Materials, Vol.**31**(1999),pp. 431-447.

[46] R. W. Jackson, M. R. Begley, Critical cooling rates to avoid transient-driven cracking in thermal barrier coating (TBC) systems. International journal of solids and Structures, Vol.**51**(2014), pp. 1364-1374.

[47] L. G. Zhao, T. J. Lu, N. A. Fleck, Crack channelling and spalling in a plate due to thermal shock loading. Journal of the mechanics and Physics of Solids, Vol.**48**(2000), pp. 867-897.

[48] R. W. Jackson, E. M. Zaleski, D. L. Poerschke, B. T. Hazel, M. R. Begley, C. G. Levi, Interaction of molten silicates with thermal barrier coatings under temperature gradients, Acta Materialia, Vol.**89**(2015), pp. 396-407.

[49] S. J. Zhang, Z. Q. Liu., An analytical model for transient temperature distributions in coated carbide cutting tools. International Communications in Heat and Mass Transfer, Vol.**35**(2008), pp. 1311-1315.

[50] A. Yevtushenko, M. R. Klosinska, The Effect of the Time Structure of Laser Pulse on Temperature Distribution and Thermal Stresses in Homogeneous Body with Coating, in Laser Pulse Phenomena and Applications, (2010), pp. 3-60.

[51] S. J. Zhang, Z. Q. Liu, Analytical and numerical solutions of transient heat conduction in monolayer-coated tools. Journal of Materals Processing Technology, Vol.**209**(2009),pp. 2369-2376.

[52] K. Ramadan, M. A. Al-Nimr, Analysis of transient heat transfer in multilayer thin films with nonlinear thermal boundary resistance. International Journal of Thermal Sciences, Vol.**48**(2009),:pp. 1718-1727.

[53] M. Y. He, D. R. Mumm, A. G. Evans, Criteria for the delamination of thermal barrier coatings: with application to thermal gradients. Surface & Coatings Technology, Vol.**185**(2004), pp. 184-193.

[54] C. Courcier, V.Maurel, L.Remy, S. Quilici, I. Rouzou, A. Phelippeau, Interfacial damage

based life model for EB-PVD thermal barrier coating. Surface & Coatings Technology, Vol.**205** (2011),pp. 3763-3773.

[55] N. Curry, Z. L. Tang, N. Markoscan, P. Nylen, et al., Influence of bond coat surface roughness on the structure of axial suspension plasma spray thermal barrier coatings — Thermal and lifetime performance. Surface and Coatings Technology, Vol.**268** (2015),pp. 15-23.

[56] S. A. Tsipas, I. O. Golosnoy, R. Damanl, T. W. Clyne, The Effect of a High Thermal Gradient on Sintering and Stiffening in the Top Coat of a Thermal Barrier Coating System. Journal of Thermal Spray Technology, Vol.**13** (2003),pp. 370-376.

[57] J. A. Nesbitt, Thermal modeling of various thermal barrier coatings in a high heat flux rocket engine. Surface and Coatings Technology, Vol.**130**(2000),pp. 141-151.

[58] M. Marr, and O. Kesler, Influence of plasma heat flux on segmentation cracking and permeability of thin suspension plasma sprayed coatings. Surface and Coatings Technology, Vol.**216** (2013),pp. 289-296.

[59] J. L. Smialek, Compiled furnace cyclic lives of EB-PVD thermal barrier coatings. Surface & Coatings Technology, Vol.**276**(2015),pp. 31-38.

[60] T. Beck, R. Herzog, O. Trunova, M. Offermann, R. W. Steinbrech, L. Singheiser, Damage mechanisms and lifetime behavior of plasma-sprayed thermal barrier coating systems for gas turbines — Part II: Modeling. Surface & Coatings Technology, Vol.**202** (2008), pp. 5901-5908.

[61] Robert VaBen, M.J.T.S., Surface & Coatings Technology. Surface & Coatings Technology, Vol.**205** (2010), pp. 938-942.

[62] K. S. Chan, Cyclic-Oxidation Resistance of Niobium-Base in situ Composites: Modeling and Experimentation. Oxidation of Metals, Vol.**61** (2004), pp. 165-194.

[63] J. L. Smialek, A deterministic interfacial cyclic oxidation spalling model. Acta Materialia, Vol.**51**(2003),pp. 469-483.

[64] Deepa Mudgal, S. Singh, S. Prakash, High Temperature Cyclic Oxidation Behavior of Ni and Co Based Superalloys, Journal of Minerals &Materials Characterization

&Engineering, Vol.**11**(3)(2012),pp. 211-219.

[65] B. M. Gleeson, B. T. Li, Cyclic Oxidationof Chromia-Scale Forming Alloys: Lifetime Prediction and Accounting for the effects of Major and Minor Alloying Additions. Materials Science Forms, Vol.**461**(2004), pp.427-438.